Master's thesis

NTNU
Norwegian University of Science and Technology
Faculty of Natural Sciences
Department of Physics

Iacob Fleischer Nedreaas

SpiderCat - A Catalog of Compact Binary Millisecond Pulsars

Master's thesis in MSPHYS
Supervisor: Manuel Linares
May 2024

NTNU
Norwegian University of
Science and Technology

Iacob Fleischer Nedreaas

SpiderCat - A Catalog of Compact Binary Millisecond Pulsars

Master’s thesis in MSPHYS
Supervisor: Manuel Linares
May 2024

Norwegian University of Science and Technology
Faculty of Natural Sciences
Department of Physics

NTNU
Norwegian University of
Science and Technology

NTNU
Kunnskap for en bedre verden

Department of Physics

FY3900 - Master Thesis in Physics

SpiderCat - A Catalog of Compact Binary Millisecond Pulsars

Author:
Iacob Fleischer Nedreaas

May, 2024

Abstract

In this thesis, we present a catalog of compact binary millisecond pulsars (CBMSPs), also known as “spiders”. We start with an introduction to neutron stars (NSs) in general and CBMSPs in particular: their formation, structure, and evolution. We use existing NS and multi-wavelength catalogs to compile and complement our own catalog: SpiderCat. We include all known spiders in the Galactic disk, confirmed or candidate (currently 76). From an initial updated list of CBMSPs, we searched several existing databases to obtain information regarding the timing, astrometric and photometric properties of each system. We also search and analyze the main properties of the interstellar medium in each line of sight.

First, we inspect the timing properties such as the NS spin period, its time derivative, the orbital period and other orbital properties. These data are collected from the pulsar catalog maintained by the Australia Telescope National Facility, using a self-developed script in Python. In Chapter 3, we turn to the interstellar medium and, in particular, to how dust, gas, and free electrons impact the observations of spiders through reddening, absorption, and pulse dispersion, respectively. Chapter 4 presents the astrometric properties of our systems. Using two optical surveys, we find optical counterparts for more than half of the spiders in our sample. We also tabulate and plot the parallaxes and proper motions of these systems. Chapter 5 presents the photometric properties in the optical and X-ray bands. This includes optical magnitudes, color indices and X-ray fluxes.

The main findings of this thesis are i) the confirmation of the fact that spiders host the fastest-spinning NSs, ii) the finding that redbacks display a higher proper motion than black widows and iii) the confirmation of an extreme companion temperature for PSR J1816+4510. To conclude, we provide an overview of the catalog and discuss future improvements.

Acknowledgments

I would like to express my gratitude to NTNU for giving me the opportunity to get a Master's degree in physics. The largest and sincerest thanks are dedicated to my supervisor, Prof. Manuel Linares. His guidance, advice, and knowledge in the making and writing of this thesis have made this possible. He has repeatedly shown patience and academic professionalism, which I admire. I would particularly thank him for providing support beyond his working hours on paternity leave.

I would also like to thank the LOVE-NEST research group for providing me with insight into their work in the weekly meetings and for helping me better understand the details of their work that are applicable to this thesis. Through this group, I have learned about a lot of the research done on CBMSPs. My thanks are also extended to the senior engineer in the group, Bogdan Voaidas, who has helped with various issues related to software and hardware.

Thanks also to the Department of Physics and the Faculty of Natural Sciences for providing me with the necessary equipment to complete the thesis. In particular, I am grateful for the designated desk and computer that I use in my work.

Finally, I would like to express my sincere gratitude and love to my family and friends. The time I spent as a student was fulfilling due to the love I received from them. The support and love I received from my mom and dad, in particular, have been a major reason for me to keep going in times of hardship. To Adrian Larsen and Gaute Eng Simonsen, I express my gratitude for all the extracurricular activities that we have shared and for making my time far more enjoyable.

Contents

List of Figures

List of Tables

Chapter 1

Introduction

1.1 Neutron stars

The first neutron star (NS) ever detected was discovered in the 1960s. Using the Mullard Radio Observatory, Hewish et al. [1] detected a periodic pulsation. The scientists who made the discovery were initially surprised by such a stable periodic signal. Consequently, they named the source LGM-1, which stands for Little Green Men 1, because they jokingly discussed the possibility that the signal was alien in origin. Later, it was concluded that LGM-1 was the first observation of a NS [1].

NS have small radii (8-20 km) yet large masses in the range 1-3 $M_\odot$, making them one of the densest objects in the universe. The name neutron stars comes from being prevented from collapse because of the neutron degeneracy pressure and are incredibly neutron-rich.

1.1.1 Formation of neutron stars

The evolution of a star is primarily determined by its mass. As seen in Figure 1.1, there are several stages of the evolution of a star. NSs are the final evolutionary state for stars with an initial mass in the range 9.5-25 $M_\odot$ [2]. Stars with these masses will fuse the lighter elements up to iron, where there is no longer an energy release from fusion because iron is the element with the tightest bound core. Given that the heavier elements are formed in the star's center, an iron core will ultimately develop. When the iron core reaches the Chandrasekhar limit of around 1.4 $M_\odot$, the electron degeneracy pressure supporting the core from collapse is no longer strong enough to support the total mass of the iron core [2]. Consequently, the core collapses into a proto-NS. A supernova will shed the star's outer layers in the explosion, leaving only the core and a supernova remnant. The core will collapse until electrons and protons overcome the energy threshold to produce a neutron and a neutrino. The collapsed core then has one of two fates, a black hole or a NS. The fate of the collapsed core is determined by the remaining mass. If the collapsed core's mass is less than $3M_\odot$, it will become a NS [3].

1.1.2 Neutron star structure

A NS can be divided into the following layers: the atmosphere, the outer crust, the inner crust, the outer core, and the inner core. The structure of a NS is visualized in Figure 1.2, where we can see the distinctions between the different layers of the NS. The atmosphere represents a thin plasma layer where the spectrum of a NS thermal electromagnetic radiation is generated [4]. The thickness of the atmosphere is dependent on the NS temperature but ranges from 0.1 cm to 10 cm.

The outer crust just below the atmosphere extends down a few hundred meters. In the outer crust,

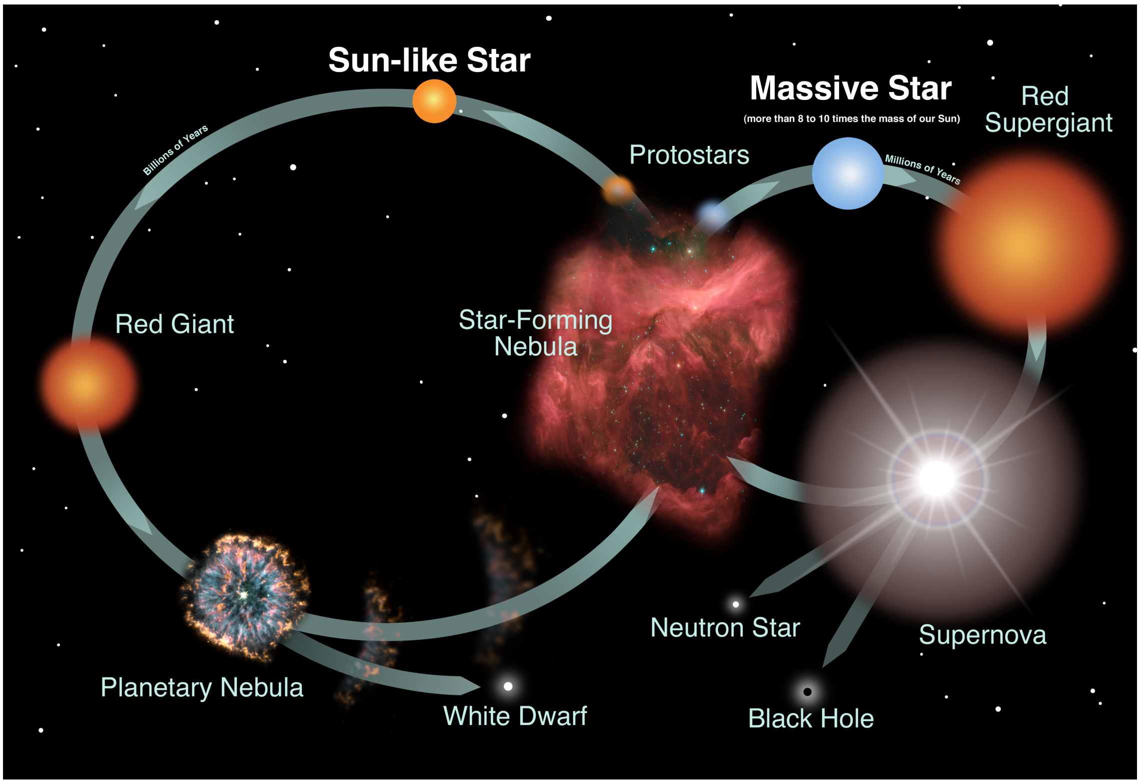

Figure 1.1: A diagram showing some of the different evolutions of stars, including NS. The figure includes main sequence stars, red giants, proto-stars, white dwarfs and black holes and gives a simplefied evolutionary path for these stars. Credit: NASA Goddard Flight Space Center.

the density is around 10^6 g cm^{-3}. The crust is mainly composed of ionized atoms, and the density is so high that the electrons behave like a degenerate gas. The density is so high at the bottom of the outer crust that electrons undergo reverse β decay, creating a free neutron gas. This is the neutron drip line and marks the separation between the outer and inner crust [4].

The inner crust has a thickness of about $10^4 cm$, and the density reaches half of the nuclear matter saturation density ($\rho_s = 2.7 * 10^{14}$ g cm^{-3}; [5]). The inner crust contains a lot of neutron-heavy atomic nuclei as well as free neutrons. At the separation of crust and core, nuclei and free neutrons disappear in a superfluid state. [4]

The equation of state is not known specifically in the core of a NS. Still, it is believed that the remaining free electrons are forced together with the protons producing neutrons and muons, making the core incredibly neutron-rich. The density in the core is in the range $3.5 * 10^{14}$ g cm^{-3} to $1.4 * 10^{15}$ g cm^{-3} [4], higher than the density of atomic nuclei.

In the inner core, the density becomes even higher. The inner core has a radius of several kilometers. There are multiple hypotheses regarding the composition of the inner core. These include hyperonization of matter, pion condensation, kaon condensation and a phase transition to quark matter [4].

1.2 Millisecond pulsars

Some NSs are emitting electromagnetic radiation from their magnetic poles. We call these NSs pulsars. Pulsars are spinning around their rotational axis, which usually is different from their magnetic axis. From Earth's perspective, pulsars appear as pulsating light sources as their radiation beams sweep across our line of sight. Millisecond pulsars (MSPs) have a rotational period of $P <$ 30ms, making them the fastest spinning NS. Due to the extreme properties of a MSP, they become

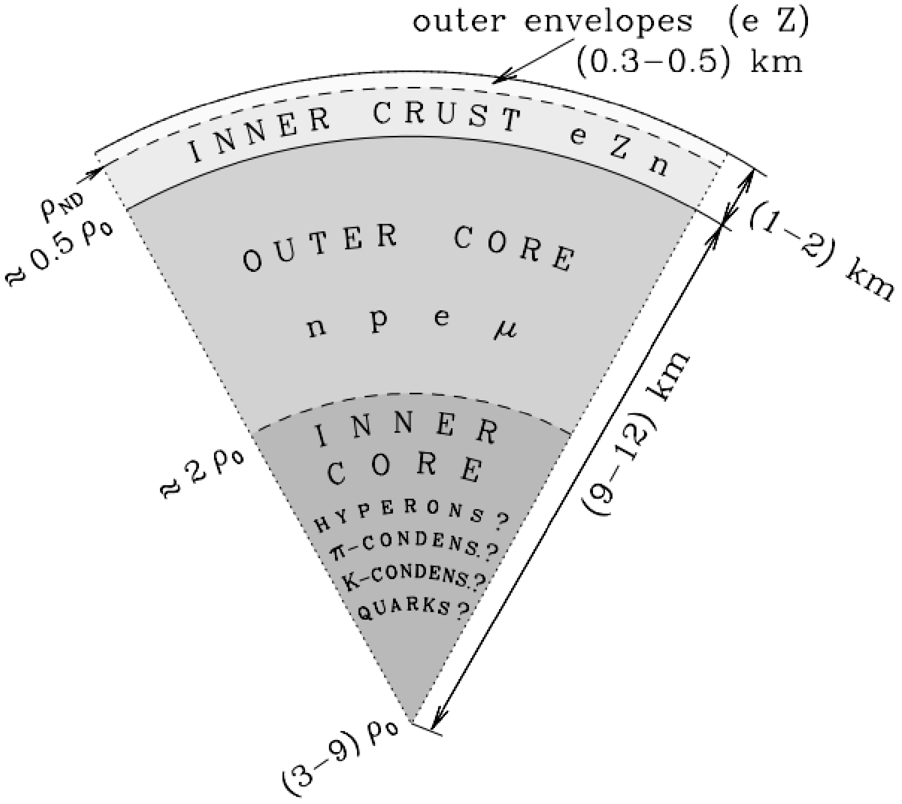

Figure 1.2: Schematic displaying the structure of a NS. This structure is divisible into outer envelopes, inner core, outer core and inner core. The figure also shows a typical scale and the density borders between the different layers. Credit: Haensel 2007 [4]

unique laboratories with densities and magnetic fields impossible to create on Earth.

The first MSP was discovered in 1982 by Becker et al. (B1937+20 with a spin period (P) of 1.6ms [6]). This was an unexpected discovery as all other discovered pulsars had significantly longer P up to that point, thus challenging the models for NS formation and especially the evolution of MSPs.

The $P{-}\dot{P}$ diagram, shown in Figure1.3, is a pivotal tool in pulsar astronomy, mapping P against the spin period derivative ($\dot{P}$) for a population of pulsars. The pulsar period, P, is on the horizontal axis in seconds. P is defined as the time the pulsar uses to complete one rotation around its rotational axis. The vertical axis represents the dimensionless $\dot{P}$, often quoted in seconds per second (s s^{-1}). $\dot{P} = \frac{dP}{dt}$, quantifies the the stability of the rotation. Pulsars occupy distinct regions on this diagram, with younger, more energetic pulsars exhibiting longer periods and higher period derivatives, while older, recycled MSPs gather in the region of short periods and lower period derivatives. In this bottom-left corner of the $P - \dot{P}$ diagram, we find MSPs in general and, in particular, spiders.

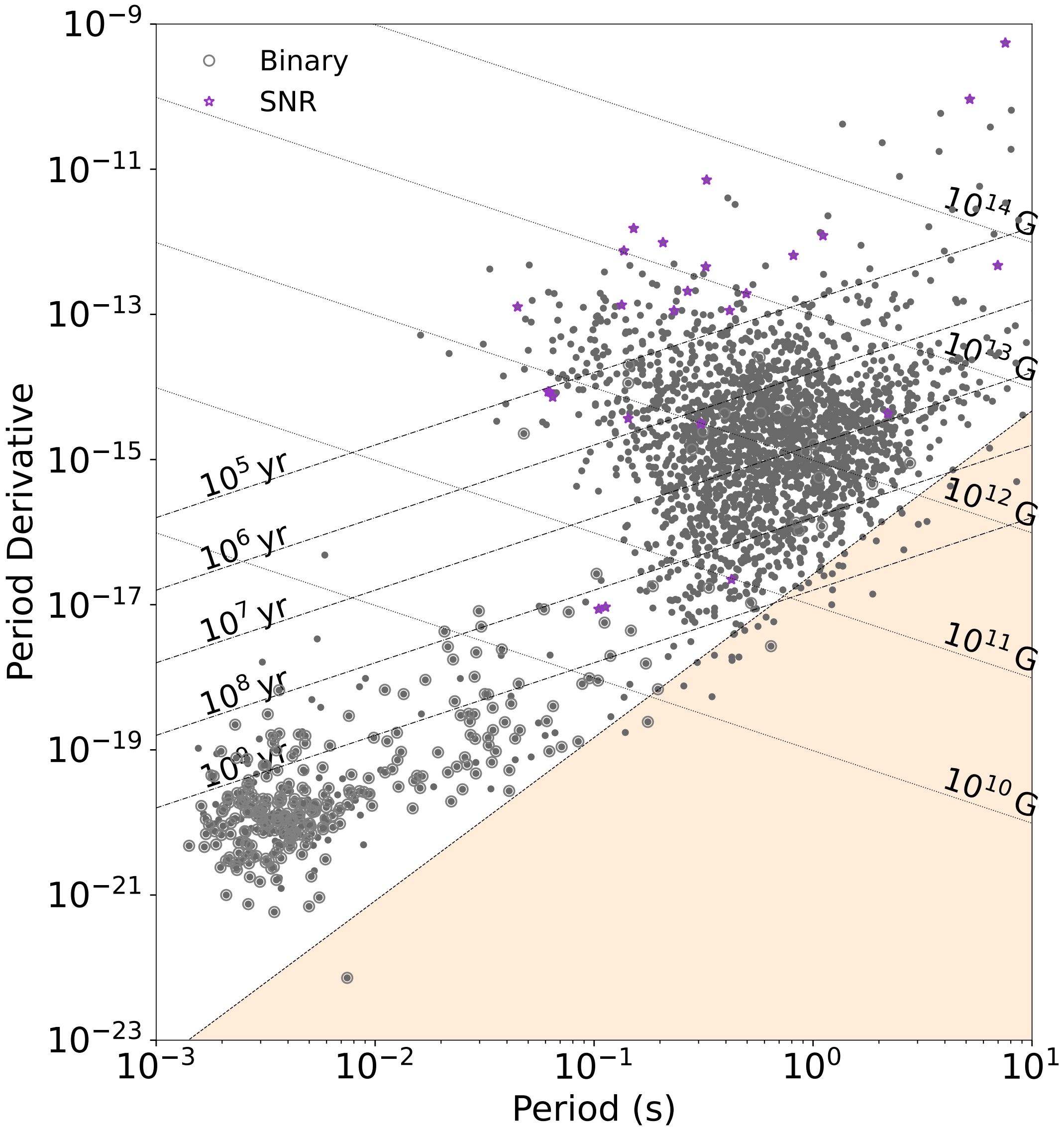

Figure 1.3: A $P - \dot{P}$ diagram displaying the pulsars in ATNF as of 22.05.24. The beige-shaded section shows the pulsar graveyard. The diagram also features lines of equal magnetic field strength and characteristic age of pulsars. The diagram separates binary pulsars and those found in supernova remnants.

1.3 Spiders

Spiders are a subset of MSPs. Their scientific name is compact binary millisecond pulsars (CBMSPs). They are also known within the astrophysical community as spiders, named after two arachnid species because of their tendency to consume their companions. These are redbacks and black widows, two arachnid species in which the females consume their partner after mating. The difference between redback and black widows is explained below.

Even though the first pulsar was discovered in 1962 and the first CBMP B1957+20 was discovered in 1988, the population of spiders remained small until 2009. As Figure 1.4 shows, after the launch of Fermi in 2008 [7], there is an immediate increase in the number of discoveries per year. The increased known population of spiders has led to a booming field of research in astrophysics. The research conducted on CBMSPs would not have been as prominent without the observations from

Fermi.

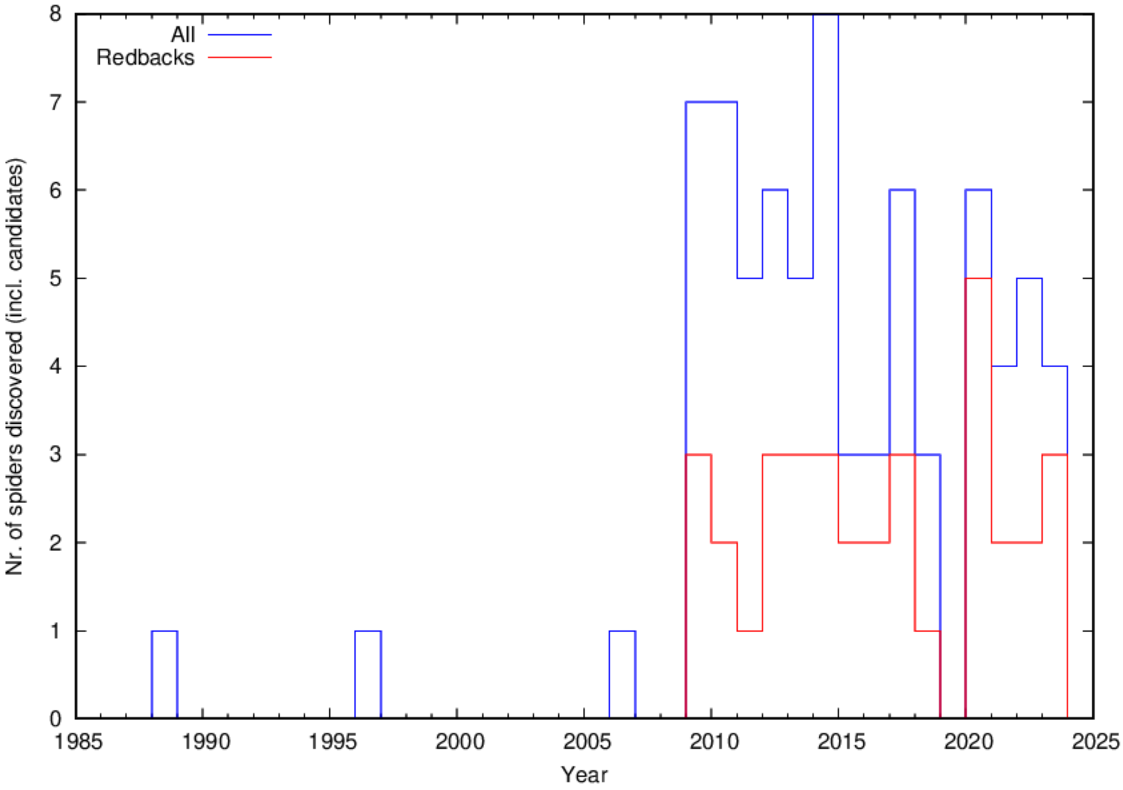

Figure 1.4: A histogram displaying the discovery rate of redbacks and all spiders, including candidate discoveries. Since redbacks and black widows make up all the spiders, the difference between all spider discoveries and redback discoveries is the discoveries of black widows. Note the increase after Fermi launched in 2008 [7]. Data collected from galMSP [8].

Spiders are highly interactive systems due to their compact orbits. The pulsar's winds and high-energy radiation can strongly influence the radii and surface properties of the companion stars. The term "state of a spider" refers to the classification system used to describe the various physical states that a spider can occupy. One state is the pulsar state. In this state, the pulsar rotates with a stable period and emits beams of radiation, mainly in the radio band. Another state is the disk state. In this state, the interaction with the companion is more significant. The disk state is characterized by the transfer of matter from the companion into a disk orbiting the pulsar. This accretion disk leads to higher energy fluxes in the X-ray and γ-bands. The outburst state is another state. This state occurs when the mass accretion rate onto the NS is high; then the pulsar can become an X-ray transient, and the X-ray luminosity can increase by several orders of magnitude. The outburst state has only been observed in one redback in a globular cluster outside of the Galactic disk so far, so it is not included in our catalog.

Redbacks are characterized by their irregular eclipsing phenomena and the presence of a non-degenerate companion star, typically a main sequence star. The typical companion in a Redback system is a low-mass star, often with a mass of about 10% of the pulsar itself, which typically fills its Roche lobe. Due to the interactions with their companion, both redbacks and black widows display radio eclipses [9].

Black widow systems feature extremely low-mass companions ($M_C \simeq 0.01 M_p$), typically only a few percent of the pulsar's mass, which are subjected to intense radiation and relativistic particle wind from the pulsar. This relentless bombardment can lead to the eventual evaporation of the companion star, potentially leaving behind an isolated MSP. This is the process by which we believe all isolated MSPs have been formed [10].

1.4 Neutron star catalogs

In this work, we have made extensive use of 2 previously compiled and frequently updated pulsar catalogs: The Australia Telescope National Facility catalog (ATNF) [11] and Galactic millisecond pulsars (gal MSP) [8]. Not all spiders are contained in the disk of our Galaxy, and some spiders reside in globular clusters. A globular cluster is a group of stars with a high number density of stars outside of the Galactic disk. In this thesis, we do not include these systems, and we focus on CBMSPs in the field of our Galactic disk. For completeness and to compare with the spider population in globular clusters, we also summarize here the catalog of pulsars in globular clusters.

1.4.1 ATNF

The ATNF database is the most comprehensive of the existing pulsar catalogs. It contains 3534 pulsars [11]. Established in the 1990s, the database has been instrumental in consolidating pulsar data from observations around the world. The list of parameters in the ATNF database is long, but some of the main ones of interest are the timing parameters, including P and $\dot{P}$. The ATNF database is updated on average every three months with pulsar discoveries. The ATNF database is accessible within Python using the PSRQPY package [11]. For these reasons, this work will collect timing properties from the ATNF database for the CBMSPs. For more information about the ATNF database, see Section 2.3.

1.4.2 Galactic millisecond pulsars

The Galactic Millisecond Pulsars (galMSP) database was initially compiled by Duncan Lorimer and contains 552 MSPs. The galMSP database is now maintained by Elisabeth Ferrara from the University of Maryland. The database includes name, P, dispersion measure (DM), orbital period, Galactic coordinates, projected semi-major axis, and the date and reference for discovery [8]. The galMSP database was used in this thesis to collect the discovery year and method of discovery. It also serves as the source for Figure 1.4. The current version (as per 22.05.2024) of the galMSP catalog contains all of the confirmed black widows but none of the four candidates. The galMSP also includes all the currently confirmed redbacks, except for J0212+5320, which was confirmed in 2023 by Perez et al. [12]. In addition, ten redback candidates do not appear in the galMSP database.

1.4.3 Pulsars in globular clusters

The globular cluster pulsars database contains 314 pulsars located in 41 different globular clusters [13]. As the name suggests, the catalog is divided based on which globular cluster the pulsar resides in. The number of known pulsars in the different clusters varies from 49 pulsars in the cluster Terzan 5 to several clusters with only one pulsar known. The database contains the name, P, $\dot{P}$, angular distance from the cluster, DM, orbital period, projected semi major axis, eccentricity, companion mass, notes and references. This is in addition to properties related to the cluster in which each pulsar resides. The catalog is a product of Paolo Freire's work and is regularly updated. It is limited to globular clusters, so pulsars that exist outside of these known globular clusters are not included in the catalog. The catalog contains 17 redbacks from 10 different globular clusters. Freire has also identified 36 black widows from 15 globular clusters [13]. These are spiders that are not in SpiderCat due to the fact they reside in globular clusters and not in the Galactic disk.

1.5 This work

The purpose of the Spider Catalog (SpiderCat) is to have a centralized database for all spiders in the Galactic disk, containing relevant properties that are available. This includes timing properties, interstellar medium (ISM) properties, astrometry data and photometry data. The SpiderCat is meant to be a regenerative database, meaning it is semi-autonomously updated. By adding the pulsar name and position whenever a new spider is discovered and running the specified Python scripts, the SpiderCat will rebuild itself with the latest discoveries.

The script requires some manual input and literature searches. When this is needed, it is specified in the READ.ME file that will accompany the script for the SpiderCat. This thesis serves as a data mining endeavor aiming to collect and compare all the relevant observations on the population of CBMSPs in the Galactic field.

The SpiderCat now contains 76 spiders, 40 of which are black widows and 36 redbacks. This includes four black widow candidates without detected of pulsations and 14 redback candidates. During the making of this thesis, there have been four redbacks and one black widow have either been confirmed or discovered as a candidate.

The fundamental basis of the SpiderCat is the ‘base file’. From this, the catalog is extended to its entirety. This base file includes only the most basic information about the spider. The name, position, discovery year, discovery note, if the spider is confirmed or just a candidate and state. From this starting point, the catalog is formed using various methods, which will be discussed in upcoming chapters. The credit for making the .BASE FILE goes to Prof. Manuel Linares, who has compiled and updated (since 2013) a catalog of spiders in the Galactic field.

Chapter 2

Timing Properties

2.1 Measured timing properties

When a new pulsar is discovered, the first measured property is P. In some cases, the presence of a MSP can be inferred indirectly from the optical properties of the companion star and/or the X-ray emission from the inter-binary shock. These systems are called “spider candidates”, and the spin properties of the MSP remain unknown until pulsations are discovered. P is used in many of the derived properties, so an unknown P will also lead to some unknown derived properties (see Section 2.2). $\dot{P}$ has been defined in Chapter 1.

DM is not a timing property in itself but rather an ISM property. However, it affects timing measurements by broadening an otherwise sharp pulse when adding multiple frequency channels, which are dispersed by different amounts. In actual physical terms, the DM is an integral number density along the line of sight of free electrons [14]. For more on this, see Section 3.3.

P_b is the orbital period of the pulsar in the binary system. Given that the NS is far more massive than the companion, the center of mass of the binary system is much closer to the NS, so its orbital velocity is significantly less than that of the companion. P_b is the time it takes for the spider and the companion to complete one revolution around the center of mass. For spiders this quantity is often given in units of days, implying that the orbit is compact and the distance between the two stars is small.

The time of the ascending node (T_{asc}) marks a specific moment in the orbital motion of an object when it passes through the ascending node, moving from below the plane of reference to above it, as seen in Figure 2.1. This plane of reference is usually perpendicular to the line of sight from the observer, known as the plane of the sky for astronomical observations. T_{asc} is the moment when the object has the highest radial velocity (positive receding). The radial velocity of the pulsar is determined by measuring the Doppler shift of the emitted pulses.

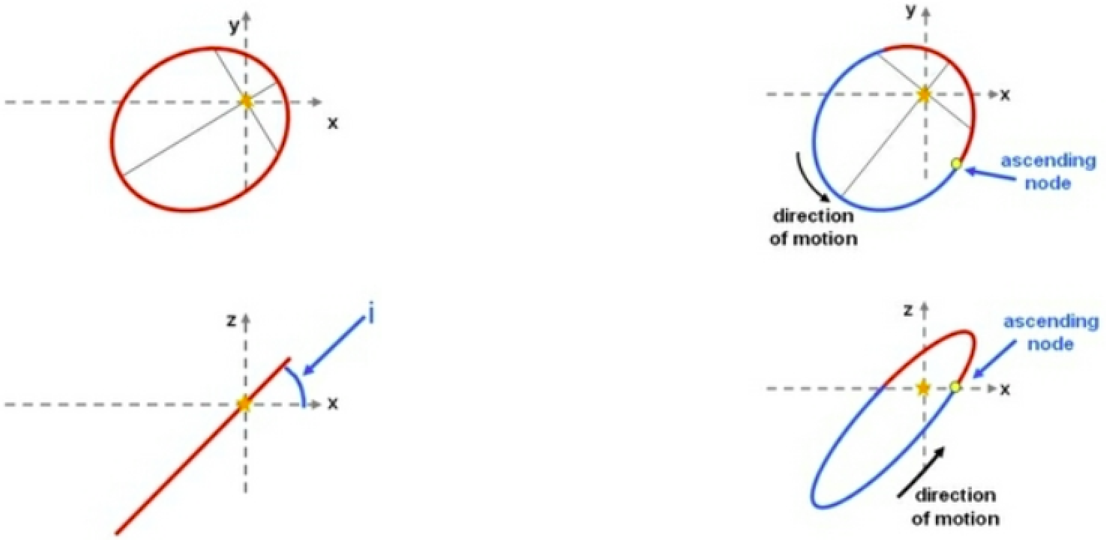

Figure 2.1: An illustration of the T_{asc} and the orbital inclination (i). In this illustration, the line of sight is The z-axis for all four figures. The top row of elliptical orbits shows the xy-plane (as seen from Earth), while the bottom row displays the same orbits from a sideways view. Credit: [15].

The projected semi-major axis (A_1) describes the apparent projected size of the orbit. The semi-major axis is the longest radius of an ellipse, representing half the longest diameter. The inclination of the orbit can be estimated through optical modeling. The inclination of the orbit is the angle between the plane of the sky and the plane of the orbit, as seen in Figure 2.1.

2.2 Derived timing properties

In addition to the measured NS spin properties, if we know or assume the moment of inertia I of the NS, we can calculate the spin-down luminosity of the pulsar. The moment of inertia is assumed to be that of a homogeneous sphere and is given by $2MR^2/5$. The radius and mass of the observed pulsars are, in general, unknown quantities. For our derived properties, we assume that all pulsars have a mass $M_p = 1.4\mathrm{M}_\odot$ and a radius of 11 km [16]. The Rotational energy [17]

$$E = \frac{I\omega^2}{2} = \frac{2\pi^2 I}{P^2}, \tag{2.1}$$

where ω is the angular frequency, is the energy associated with the rotation of the NS. We often use the first time derivative of the rotational energy. This quantity is called the spin-down luminosity

$$\dot{E} = -\frac{dE}{dt} = \frac{4\pi^2 I\dot{P}}{P^3}, \tag{2.2}$$

and sets the total power budget of the pulsar. When the pulsar rotates, so does its magnetic field. To estimate the magnetic field strength at the NS surface, we must know P, $\dot{P}$ and the angle between the magnetic and rotational axes, α. The magnetic field strength can then be expressed as [17]:

$$B^2 = \frac{3c^3 I\dot{P}P}{8\pi^2 R^6 \sin^2\alpha}. \tag{2.3}$$

If we want to estimate the magnetic field strength at the surface, we set α to 90° so that the surface field becomes;

$$B_{surf,min} = (\frac{3c^3 I\dot{P}P}{8\pi^2 R^6})^{1/2}. \tag{2.4}$$

Kepler's laws of planetary motion impose constraints on the masses of the pulsar, and the companion, M_C. These constraints come from measurement of A_1 and P_b, and are expressed by[17]:

$$\frac{(M_C \sin i)^3}{(M_C + M_p)^2} = \frac{4\pi^2 A_1^3}{T_0 P_b^2}. \tag{2.5}$$

Here, T_0 is a constant equal to $GM_\odot/c^3$. On the right-hand side of the equation are all the measured properties. Given that there are three unknown variables on the left-hand side, we are forced to make assumptions on two of the variables. In this case, we assume that the NS mass is $1.4M_\odot$, a common assumption in pulsar astronomy. The second assumption is that the orbital inclination i is 90°. These assumptions give a lower limit on the companion mass. The constraint on the $M_{C,min}$,

$$\frac{M_{C,min}^3}{(M_{C,min} + 1.4M_\odot)^2} - \frac{4\pi^2 A_1^3}{T_0 P_b^2} = 0, \tag{2.6}$$

has now been reduced to one equation with one unknown. Knowing the minimum value for the companion mass, $M_{C,min}$, gives us insight into the system's dynamics and is the major factor in classifying the system as a redback or black widow (see Chapter 1).

2.3 ATNF

To access the data in ATNF through Python, we use the PSRQPY package [18], designed to query the ATNF pulsar catalog. The package provides an efficient and convenient way to access the data contained in the database.

As a part of the PSRQPY package is the class QueryATNF. This class has integrated query capabilities and allows for adjustable inputs and outputs. It also allows for some limits to be set on the query, so the output only returns systems that meet the criteria set in the query. This includes limiting the parameters that are outputted.

We also used the integrated PSRQPY $P - \dot{P}$ diagram. Given the importance of the diagram in pulsar astronomy, the developers [11] integrated an option to plot a selection of pulsars in the diagram. This was used explicitly for Figure 1.3, which includes the entire pulsar population in ATNF with a listed P and $\dot{P}$. Along with the timing properties, the diagram also shows whether the pulsar is isolated in a binary system or in a supernova remnant.

We list in Tables 2.1 and 2.2 the following properties from the ATNF catalog: P, $\dot{P}$, T_{asc}, P_b and A_1, with their errors. In addition to the timing properties, we obtained position, DM, type, name, date of discovery, binary model, and associated names from the ATNF database. Some of these parameters will be discussed in later Chapters.

The spiders in the ATNF database were searched using pre-compiled sky coordinates. We used a search radius of 1 arcminute. We did not find multiple matches within this radius; if we did, the one with the closest angular distance to the center was selected. The search radius can be justified as follows. Considering a sphere with 4000 randomly distributed points (ATNF currently lists 3534 pulsars), we can find the average angular separation between them. This gives an average angular separation of 217 arcminutes. So with a search radius of 1 arcminute, the probability of one independent spurious match is 0.0085%.

2.4 Results

Figure 2.2 shows the $P - \dot{P}$ diagram of the entire pulsar population, shows the confirmed redbacks and black widows from SpiderCat. We can see how spiders occupy the leftmost region of this diagram, showing shorter P values than the average other MSPs. Figure 2.3 shows this as well. With a noticeable shift for the spiders towards shorter spin periods. This confirms that spiders contain the fastest spinning NSs known to date. Indeed, Tables 2.1 and 2.2 show that 8 black widows (out of 33) and 3 redbacks (out of 17) have extremely short spin periods $P < 2$ ms. This is likely due to a more efficient or longer "spin-up" phase than other recycled MSPs (with white dwarf companions).

Figure 2.4 shows the relation between the estimated magnetic field strength at the surface and the spin-down luminosity. This indicates that the spiders with the lowest magnetic field strength are black widows, as the nine spiders with the lowest magnetic field strength are all black widows. The lowest value for the magnetic field strength is for pulsar J2055+3829, with a value of 9.27 10^7 Gauss. This is likely due to the evolutionary differences and accretion history between these types of systems. Black widow pulsars often have undergone more significant mass transfer, which can lead to magnetic field burial or decay as material is accreted from the companion star. As material from the companion star is accreted onto the surface of the NS, it can compress and spread the star's magnetic field lines over a larger area. This spreading dilutes the magnetic field's strength at any given point on the surface of the NS, effectively lowering the observable magnetic field strength.

In Figure 2.5, we show the defining differentiating properties of redbacks and black widows' minimum companion mass against the orbital period. The figure shows us that redback companions have a mass about one order of magnitude bigger than those of black widows. Apparent from Figure 2.5 there is a redback with orbital period > 1 day, which has been classified as a "huntsman". The idea for the huntsman spider is that they are wide compact object binaries with a helium white dwarf (instead of a main sequence-looking companion). Given the distinctive companions for black widows and redbacks there is discussion about whether they originate from the same initial population [19] of binary stars or come from different initial binaries [20].

Table 2.1 displays the values of the black widows that appear in the ATNF database. There are 33 black widows listed in Table 2.1 out of the 40 listed in SpiderCat. Table 2.2 presents the redbacks in ATNF. 17 redbacks are listed in the table, which is less than half of the population of redbacks in SpiderCat. This is partly because there are more redback candidates, which excludes 10 candidates, which leaves a set of 9 confirmed redbacks that are not in ATNF.

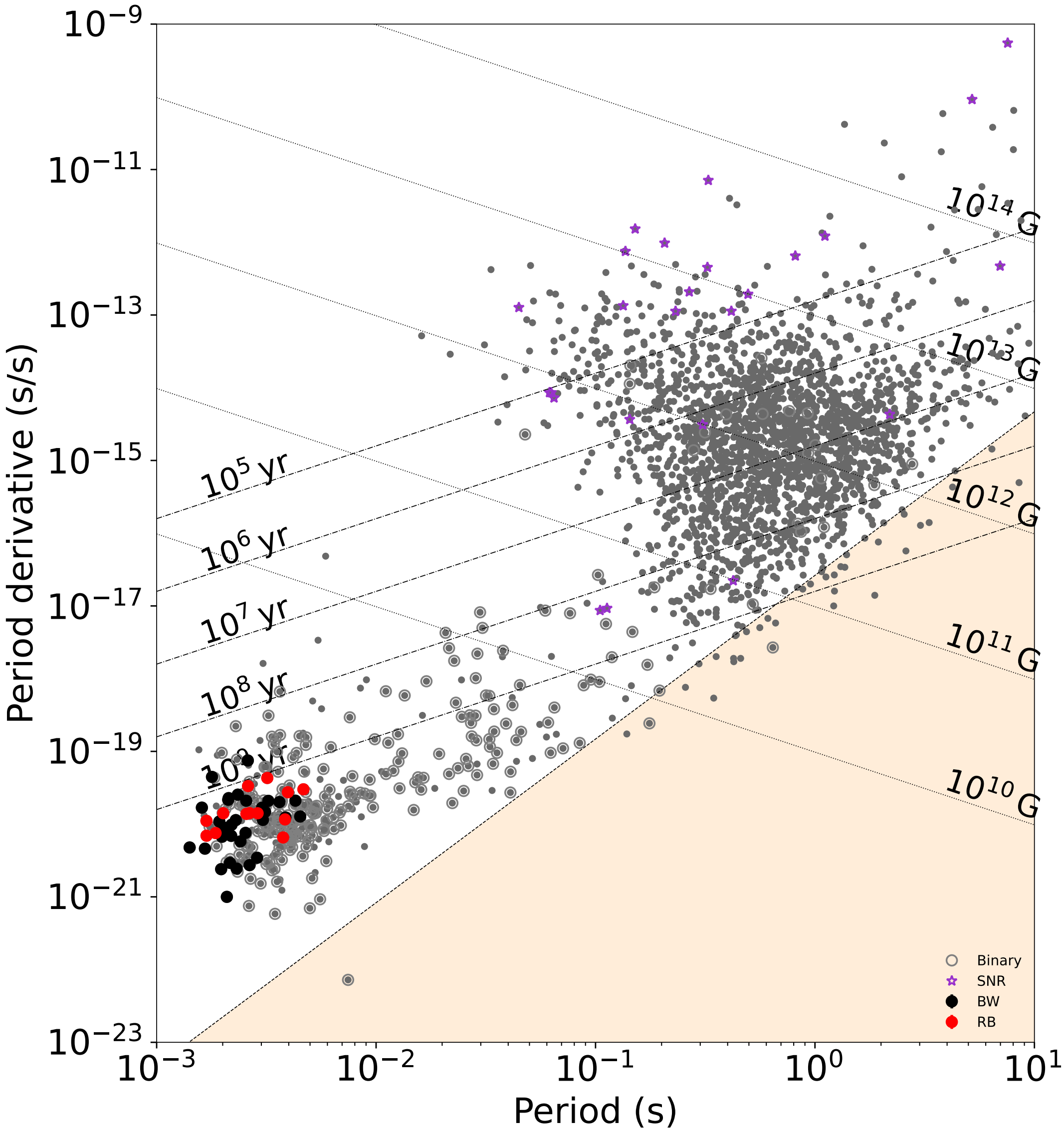

Figure 2.2: The $P - \dot{P}$ diagram of the timing properties of the spiders found in the ATNF database. This the same diagram as Figure 1.3, but here are black widows are highlighted in black and redbacks are highlighted in red. Data collected from [21].

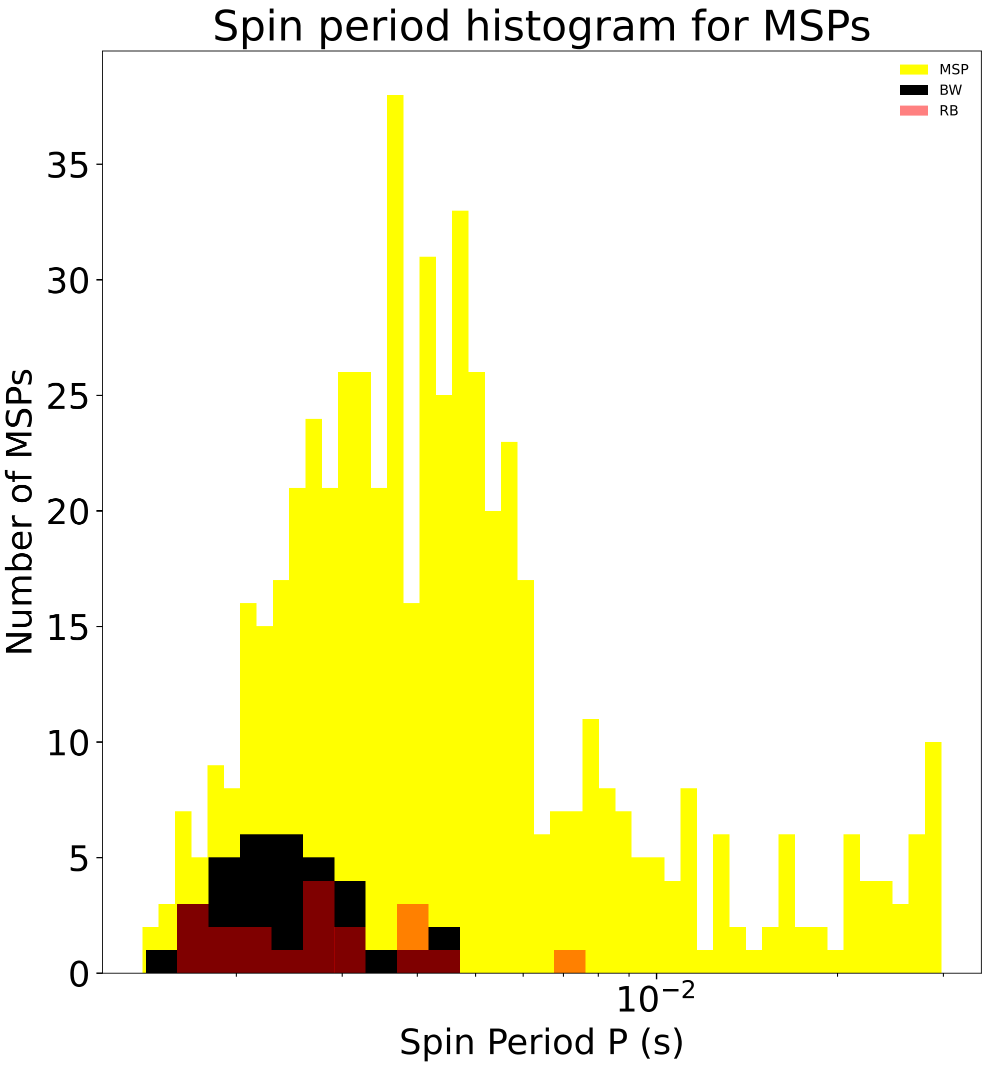

Figure 2.3: A histogram of P for the total MSP population with the as the black widows shaded black and redbacks shaded red. As there is significant difference in the population of these three groups we used different size bins for the histogram. Where the Total MSPs were divided into 50 bins the spiders were divided into 15 bins.

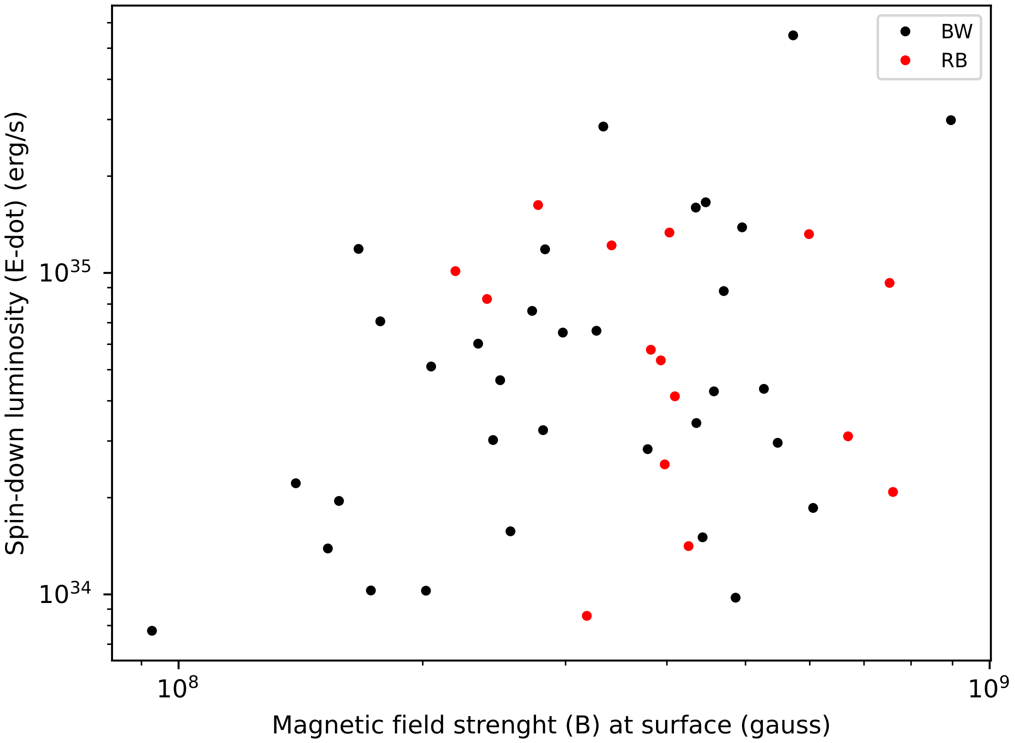

Figure 2.4: The minimal magnetic field strength at the surface against the spin-down luminosity. The magnetic filed strength is obtained by implementing the calculations and assumptions of Equation 2.4 and the spin-down luminosity is from Equation 2.2.

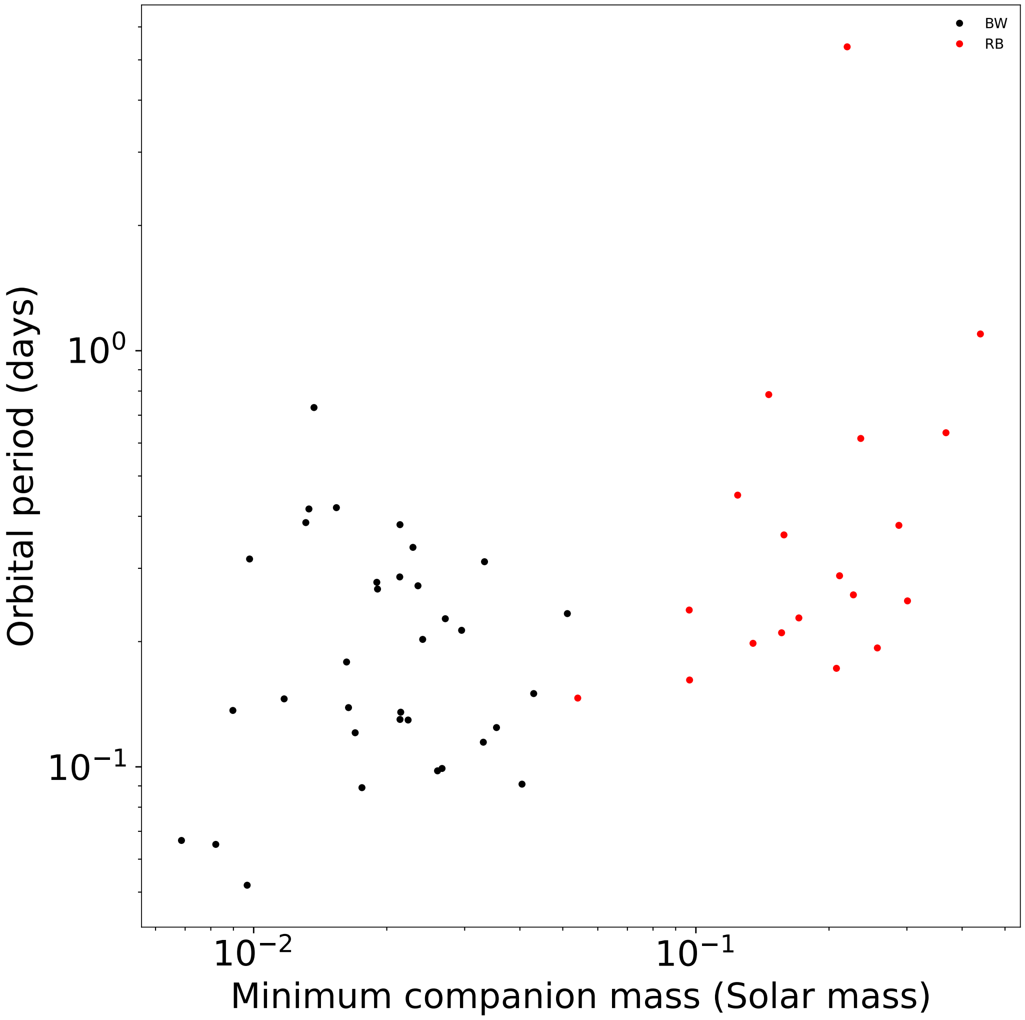

Figure 2.5: The minimal companion mass against the orbital period, expressen in $M_\odot$. Showing the defining distinction between black widows and redbacks. We can also see the huntsman redback spider with a orbital period > 1 day.

Name	P0(ms)	err	P1(s/s)	err	Tasc(MJD)	err	Pb(days)	err	A1(lt sec)	err
B1957+20	0.0016074	3e-17	1.68515e-20	9e-25	-	-	0.381967	8e-10	0.0892253	6e-07
J0610-2100	0.00386132	8.9e-17	1.23266e-20	1e-25	55699	2e-07	0.286016	3e-11	0.0734891	1.4e-07
J2051-0827	0.00450864	1e-16	1.27334e-20	6.1e-24	54091	8e-07	0.0991103	4e-11	0.045072	3e-07
J0023+0923	0.0030502	3.7e-18	1.14234e-20	1.4e-25	56845	6e-08	0.138799	3.2e-11	0.0348414	5e-08
J0251+2606	0.00254155	2.6e-16	7.57182e-21	7.1e-24	56647	5e-06	0.202441	9e-10	0.065681	8e-06
J0636+5128	0.00286895	3.3e-17	3.44901e-21	1.2e-25	56027.2	7e-07	0.0665513	6e-11	0.00898628	8e-08
J0952-0607	0.0014138	1.2e-16	4.7732e-21	8e-24	57980.4	5e-07	0.267461	5e-10	0.062667	9e-07
J1124-3653	0.00240957	8.1e-16	6.01157e-21	8.7e-24	55128.6	5e-06	0.226988	1.1e-09	0.079635	7e-06
J1221-0633	0.00193454	4.9e-16	5.26786e-21	6e-24	-	-	0.38635	4e-09	0.0552855	7e-07
J1301+0833	0.00184373	6.8e-16	1.05549e-20	6.8e-24	55536.5	1e-05	0.272352	1e-09	0.078127	1e-05
J1311-3430	0.00256037	2.6e-16	2.09645e-20	1.3e-23	56009.1	7e-06	0.0651157	7e-10	0.010581	4e-06
J1317-0157	0.00290824	1.7e-14	5.49763e-21	3.4e-22	-	-	0.0891283	2e-09	0.027795	4e-06
J1446-4701	0.0021947	1.4e-17	9.80745e-21	2.9e-25	55647.8	3e-07	0.277666	1.5e-10	0.0640123	1.5e-07
J1513-2550	0.00211907	1e-16	2.161e-20	2e-23	56728.5	6e-07	0.178635	8e-10	0.0408132	7e-07
J1544+4937	0.00215929	9.3e-17	2.79658e-21	4.7e-25	56124.8	4e-07	0.120773	8e-11	0.0328665	4e-07
J1555-2908	0.0017875	1.6e-16	4.4531e-20	6.4e-24	57785.5	3e-08	0.2335	1e-10	0.151447	1e-07
J1630+3550	0.00322916	8.3e-16	2.08758e-20	1e-22	59000.1	4e-06	0.315863	6e-09	0.036128	3e-06
J1641+8049	0.00202118	8.2e-17	8.94651e-21	8.2e-23	56220.5	1e-07	0.090874	1e-10	0.0640793	3e-07
J1653-0159	0.00196768	2e-16	2.402e-21	3e-24	56513.5	8e-06	0.0519448	4e-10	0.01071	1e-05
J1731-1847	0.00234456	1.1e-16	2.54069e-20	4.4e-24	-	-	0.311134	1e-09	0.120161	6e-07
J1745+1017	0.00265213	3.5e-16	2.72911e-21	1.4e-23	55210	2e-06	0.730241	1e-09	0.088172	1e-06
J1805+0615	0.00212891	4.5e-16	2.27582e-20	8.2e-24	57001.6	7e-06	0.336872	5e-09	0.087728	1.5e-05
J1810+1744	0.00166	-	4.6e-21	-	-	-	0.15	-	0.095	-
J1928+1245	0.00302161	5.5e-16	1.67994e-20	9.1e-23	57949	3e-06	0.136635	8e-10	0.018951	1e-06
J1946-5403	0.00271	-	-	-	-	-	0.13	-	0.0435	-
J2017-1614	0.00231429	4e-16	2.45e-21	5e-23	56704.8	2e-06	0.0978253	4e-10	0.043655	5e-06
J2047+1053	0.00428593	5.5e-16	2.08013e-20	7.3e-24	-	-	0.124289	2e-10	0.069303	3e-06
J2052+1219	0.00198526	7.9e-17	6.70366e-21	2e-24	56548.1	2e-06	0.114614	2e-10	0.061377	4e-06
J2055+3829	0.00208929	2.2e-17	9.99616e-22	4.4e-25	57900.1	6e-08	0.12959	1e-11	0.0452618	2e-07
J2115+5448	0.00260288	2e-15	7.49e-20	1e-22	56725.6	6e-07	0.135322	3e-09	0.044846	1e-06
J2214+3000	0.00311923	1.2e-17	1.47285e-20	3.9e-25	56884.8	3e-07	0.416633	1.9e-10	0.0590813	3e-07
J2234+0944	0.00362703	1.3e-17	2.01003e-20	5.3e-25	57186.1	1.6e-07	0.41966	1.7e-10	0.0684297	1.3e-07
J2241-5236	0.0021867	9.6e-19	6.89656e-21	2.9e-26	56727	2e-08	0.145672	2e-11	0.0257953	1.1e-08
J2256-1024	0.00229453	2.1e-17	1.13535e-20	9.5e-25	-	-	0.212883	6.3e-11	0.0829658	5e-08

Table 2.1: Tabulated timing properties with errors for the black widows in SpiderCat. The resulting table is the partial output from the query into ATNF.

Name	P0	err	P1	err	Tasc	err	Pb	err	A1	err
–	ms	s	s/s	s/s	MJD	MJD	days	days	lt sec	lt sec
J1023+0038	0.00168799	2.8e-16	6.9295e-21	8.5e-24	-	-	0.198096	3e-10	0.343343	3e-06
J1036-4353	0.00168011	-	-	-	59536.3	-	0.259	-	0.665	-
J1048+2339	0.00466516	4.4e-16	3.00775e-20	4.4e-23	-	-	0.250519	2.7e-08	0.83612	3e-06
J1227-4853	0.00168638	1.1e-14	1.10911e-20	1.1e-21	56700.9	2e-07	0.287888	1e-09	0.668468	4e-06
J1302-3258	0.00377085	1.7e-15	6.54089e-21	2.8e-23	55924.8	7e-07	0.784442	3e-09	0.927929	5e-06
J1306-4035	0.00220453	2e-08	-	-	-	-	1.0972	0.00016	3.1	0.5
J1417-4402	0.00266422	4e-10	-	-	57111.5	0.002	5.37372	3e-05	4.876	0.009
J1431-4715	0.00201195	9e-16	1.411e-20	3e-23	55756.1	4e-07	0.449739	7e-10	0.550061	2e-06
J1622-0315	0.00384543	4.4e-15	1.14306e-20	1.2e-22	-	-	0.161701	6.8e-10	0.219265	5e-06
J1628-3205	0.00321157	2e-15	1.19541e-20	4.1e-23	-	-	0.21	-	0.41024	3e-05
J1723-2837	0.00185573	1e-14	7.5418e-21	4.1e-22	55425.3	2e-06	0.615436	8e-09	1.22581	9e-06
J1803-6707	0.00213462	3.6e-16	1.84724e-20	8.7e-23	59021	1e-05	0.380473	8e-08	1.06191	3e-06
J1816+4510	0.0031931	2e-16	4.31e-20	1e-23	56047.5	2e-07	0.360893	2e-10	0.595405	1e-06
J1908+2105	0.00256439	5.3e-17	1.38348e-20	3.9e-24	56478.3	2e-06	0.146317	4e-10	0.116901	1.1e-05
J1957+2516	0.00396166	1e-15	2.744e-20	9e-23	56407.9	6e-07	0.238145	7e-10	0.283349	6e-06
J2039-5617	0.00265091	3.5e-16	1.41635e-20	4.2e-24	56885	2e-05	0.22798	3e-09	0.47105	1e-05
J2129-0429	0.00762	-	-	-	55702.1	1e-07	0.635227	3e-10	1.85	0.05
J2215+5135	0.00260962	6.8e-16	3.33696e-20	6.8e-22	55186.2	1e-06	0.172502	8e-09	0.468141	1.3e-05
J2339-0533	0.00288423	1.7e-16	1.4102e-20	6.7e-24	55791.9	3e-07	0.193098	3.2e-11	0.611656	4e-06

Table 2.2: Tabulated timing properties with errors for the redbacks in SpiderCat. The resulting table is the partial output from the query into ATNF.

Name	$\dot{E}$	B_{surf}	$M_{C,min}$	Distance (YMW)	Distance (NE)
-	erg/s	Gauss	$M_{\odot}$	kpc	kpc
B1957+20	2.85e+35	3.34e+08	0.021	1.7	2.5
J0610-2100	1.51e+34	4.43e+08	0.021	3.3	3.5
J2051-0827	9.77e+33	4.86e+08	0.027	1.5	1
J0023+0923	2.83e+34	3.79e+08	0.016	1.2	0.69
J0251+2606	3.24e+34	2.81e+08	0.024	1.2	0.82
J0636+5128	1.03e+34	2.02e+08	0.0069	0.21	0.49
J0952-0607	1.19e+35	1.67e+08	0.019	1.7	0.97
J1124-3653	3.02e+34	2.44e+08	0.027	0.99	1.7
J1221-0633	5.12e+34	2.05e+08	0.013	1.3	0.75
J1301+0833	1.18e+35	2.83e+08	0.024	1.2	0.67
J1311-3430	8.78e+34	4.7e+08	0.0082	2.4	1.4
J1317-0157	1.57e+34	2.57e+08	0.018	25	2.8
J1446-4701	6.52e+34	2.98e+08	0.019	1.6	1.5
J1513-2550	1.6e+35	4.34e+08	0.016	4	2
J1544+4937	1.95e+34	1.58e+08	0.017	3	1.2
J1555-2908	5.48e+35	5.72e+08	0.051	7.6	2.7
J1630+3550	4.36e+34	5.27e+08	0.0098	1.6	1.1
J1641+8049	7.62e+34	2.73e+08	0.04	3	1.7
J1653-0159	2.22e+34	1.39e+08	0.0097	-	-
J1731-1847	1.39e+35	4.95e+08	0.033	4.8	2.6
J1745+1017	1.03e+34	1.73e+08	0.014	1.2	1.3
J1805+0615	1.66e+35	4.47e+08	0.023	3.9	2.5
J1810+1744	7.07e+34	1.77e+08	0.043	2.4	2
J1928+1245	4.28e+34	4.57e+08	0.009	6.1	6.1
J1946-5403	-	-	-	-	-
J2017-1614	1.39e+34	1.53e+08	0.026	1.4	1.1
J2047+1053	1.86e+34	6.06e+08	0.035	2.8	2
J2052+1219	6.02e+34	2.34e+08	0.033	3.9	2.4
J2055+3829	7.71e+33	9.27e+07	0.022	4.6	4.4
J2115+5448	2.99e+35	8.96e+08	0.022	3.1	3.4
J2214+3000	3.41e+34	4.35e+08	0.013	1.7	1.5
J2234+0944	2.96e+34	5.48e+08	0.015	1.6	1
J2241-5236	4.64e+34	2.49e+08	0.012	0.96	0.51
J2256-1024	6.61e+34	3.27e+08	0.03	1.3	0.65

Table 2.3: Tabulated values for the derived properties of black widows. This table includes spin.down luminosity, magnetic field strength, minimum companion mass and two distance estimates. These distance estimates (based on the DM from ATNF) are discussed in greater detail in Chapter 4.

Name	$\dot{E}$	B_{surf}	$M_{C,min}$	Distance (YMW)	Distance (NE)
-	erg/s	Gauss	$M_{\odot}$	kpc	kpc
J1023+0038	1.01e+35	2.19e+08	0.13	1.1	0.62
J1036-4353	-	-	-	-	-
J1048+2339	2.08e+34	7.6e+08	0.3	2	0.7
J1227-4853	1.63e+35	2.77e+08	0.21	1.2	1.4
J1302-3258	8.58e+33	3.19e+08	0.15	1.4	1
J1306-4035	-	-	-	-	-
J1417-4402	-	-	-	-	-
J1431-4715	1.22e+35	3.42e+08	0.12	1.8	1.6
J1622-0315	1.41e+34	4.25e+08	0.097	1.1	1.1
J1628-3205	2.54e+34	3.98e+08	0.16	1.2	1.3
J1723-2837	8.3e+34	2.4e+08	0.24	0.72	0.74
J1803-6707	1.34e+35	4.03e+08	0.29	1.4	1.2
J1816+4510	9.31e+34	7.53e+08	0.16	4.4	2.4
J1908+2105	5.77e+34	3.82e+08	0.054	2.6	3.2
J1957+2516	3.1e+34	6.69e+08	0.097	2.7	3.1
J2039-5617	5.35e+34	3.93e+08	0.17	1.7	0.94
J2129-0429	-	-	-	-	-
J2215+5135	1.32e+35	5.99e+08	0.21	2.8	3
J2339-0533	4.13e+34	4.09e+08	0.26	0.75	0.45

Table 2.4: Tabulated values for the derived properties of redbacks. This table includes spin.down luminosity, magnetic field strength, minimum companion mass and two distance estimates. These distance estimates (based on the DM from ATNF) are discussed in greater detail in Chapter 4.

Chapter 3

Interstellar Medium

The ISM affects all astrophysical observations. Consequently, extensive work has been done to map the distribution of gas and dust in the ISM of our Galaxy [22, 23, 24]. With the help of the resulting databases that map the various properties of the ISM, we can correct results and infer the intrinsic fluxes of spiders. Some of these distributions are compiled as 3-dimensional maps. However, for the purposes of SpiderCat, a two-dimensional column density is sufficient. This assumption is made because spiders are typically distant stars with a distance of more than 1-2 kpc, where the column density in most lines of sight has flattened out. For this reason, we use the total column densities in the line of sight.

3.1 Dust

Dust presents a significant challenge to astronomical observations, acting as both a concealer and a modifier of celestial light. Interstellar dust composed of tiny solid particles scatters light. Reddening is the phenomenon where the light from a celestial object is scattered and absorbed by interstellar dust, causing the object to appear redder and dimmer than it intrinsically is. This process occurs because dust particles preferentially scatter shorter-wavelength (blue) light, allowing longer-wavelength (red) light to pass through with greater ease. This wavelength-dependent scattering results in an apparent change in the observed color of celestial objects towards the red part of the spectrum. Quantitatively, reddening can be expressed through the color excess, $E(B-V)$, which measures the difference in magnitude between the blue (B) and visual (V) bands due to dust. This parameter is a crucial indicator of the amount of interstellar dust along a line of sight and its effect on the light. The extinction [23],

$$R_V = \frac{A(V)}{A(V) - A(B)} = \frac{A(V)}{E(B-V)}, \tag{3.1}$$

has from previous measurements values between 2.6 to 5.5 with a mean value of 3.1 [25]. This is also the value used as the theoretical extinction value in our catalog (see Figure 3.2). As a consequence of reddening, the light emerging from the dust is redder than the light emitted from the companion. Astronomically, it complicates the accurate determination of luminosity, distances, and the intrinsic colors of stars. For pulsars and other distant sources, the light that finally reaches observers is dimmed and reddened, requiring careful correction to infer their intrinsic fluxes.

Astronomers have developed sophisticated dust maps to account for and mitigate the effects of interstellar reddening. One of the most widely used resources in this regard is the map by Schlegel, Finkbeiner, and Davis (1998), referred to as the SFD map [23]. This comprehensive work utilizes infrared observations to estimate the dust distribution across the sky, providing a valuable tool for correcting reddening in astronomical data. A more recent study gave rise to the Bayestar dust maps by Green et al. [24], is an outcome of the Pan-STARRS survey [26] representing a significant leap forward in our understanding of dust distribution. Since Bayestar is dependent on Pan-STARRS it shares it limitations, notably that it only covers north of DEC -30°, more on this in Chapter 5. Bayestar is leveraging optical and infrared data to produce a three-dimensional map of Galactic dust. These two databases for dust reddening are accessed and used in this thesis within Python using the package DUSTMAPS. The data are accessed by a position-based search, and the dust reddening in that line of sight is stored.

3.2 Gas

The ISM also contain a lot of gas, particularly hydrogen gas, which is the most abundant. Hydrogen gas is so abundant in the Galaxy that “no single sight line exists through the Milky Way where it could not be detected after only a few seconds” [22]. Hydrogen gas is another concealer and modifier of the light from the pulsar to the observer. So, we must account for the absorption effect that occurs.

Just above the ionization energy of hydrogen, 13.6 eV, in the ultraviolet, the ISM is highly opaque because the probability that a photon will ionize a hydrogen atom is very high [27]. This fundamental interaction exemplifies the principle of absorption, where a photon’s energy is consumed to liberate an electron from its atomic bound state, consequently elevating it to a continuum state. The quantum mechanical description underlying this interaction involves an electron’s absorption of a photon, leading to an instantaneous jump in energy states. Photons that are absorbed, primarily in discrete spectral lines and continua, effectively imprint signatures in absorption lines, which are instrumental in the spectroscopic analysis of astrophysical objects. The distribution of hydrogen gas in the ISM is not random. Like most other objects in the Galaxy, a much higher concentration is close to the Galactic disk, see Figure 3.1. The distribution of hydrogen gas in the Galaxy is highly structured, with dense regions concentrated in spiral arms and the galactic plane, and more diffuse components filling the interstellar medium.

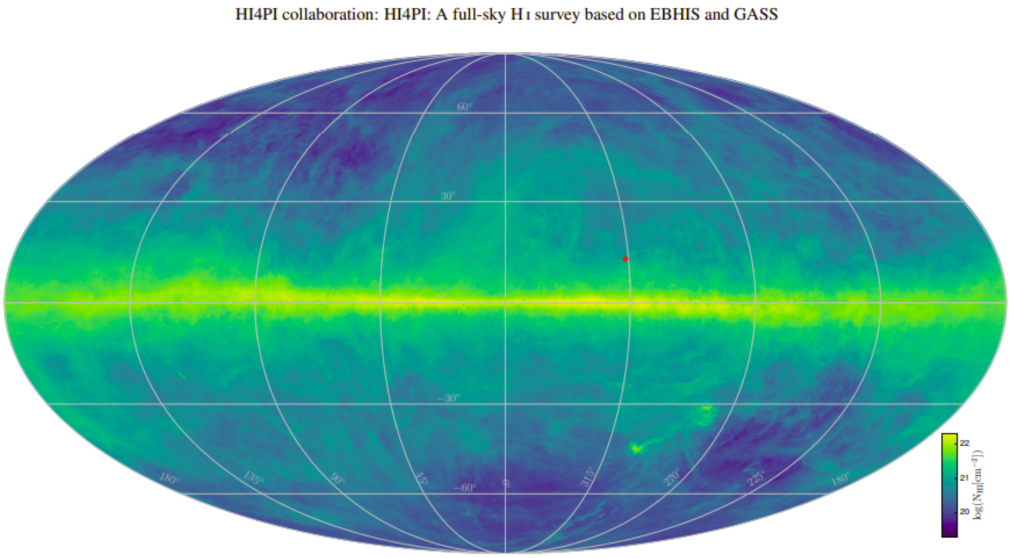

Figure 3.1: A full-sky map over the distribution of hydrogen in the Milky Way using Galactic coordinates. This shows EBHIS and GASS data as integrated over the full velocity range. The map is in Galactic coordinates using Mollweide projection. Taken from [22].

We collected the hydrogen column density data using the HI4PI database [22]. The database is a full-sky survey of the distribution of hydrogen gas. The database has been downloaded and is available on the local computers at NTNU as a part of the HEASOFT package (version 6.32.1) [28]. The HI4PI survey is based on data from the first coverage of the Effelsberg–Bonn HI Survey (EBHIS) and the third revision of the Galactic All-Sky Survey (GASS). EBHIS and GASS share similar angular resolutions and sensitivity [22]. The GASS observations were conducted from

January 2005 to November 2006, primarily at night, to avoid Solar interference, scanning each sky area twice. The EBHIS survey used the Effelsberg 100-m from late 2008 to early 2013 to cover 100 MHz of bandwidth with 16,384 spectral channels, enabling simultaneous observation of both Galactic and extra-galactic skies [22]. The query is based on position, and because HI4PI is a full-sky survey, it provides a value for every system in SpiderCat, whether the system is a candidate or a confirmed spider.

3.3 Free electrons

The DM is defined as [17]

$$DM = \int_0^d n_e \, dl, \tag{3.2}$$

where n_e is the electron number density, d is the distance to the pulsar. DM is usually expressed in units of pc cm^{-3}. Thus, DM is the total (integrated) column density along the line of sight from the observer to the star. The origin of DM comes from the interaction between electromagnetic radiation and charged particles in space. Low energy radiation, such as radio waves, is more subject to this effect since higher energy radiation goes through the ISM without being affected much. All charged particles contribute to the impact of the DM. Still, since electrons have a far smaller mass than the proton, they are more affected by the electromagnetic radiation passing by, contributing to the delay in the pulse. Therefore, only the free electron column density is considered as the cause of this effect [14]. The presence of free electrons in the ISM causes dispersion of the radio pulses from pulsars because the free electrons' refractive index varies with frequency. This leads to a frequency-dependent delay, where higher frequency waves travel faster than lower frequency waves.

The effect of the DM can be seen in a delay of frequencies where f_1 and f_2 are both in the MHz range. The time delay between the two frequencies is expressed as:

$$\Delta t \simeq D * 10^6 * (f_1^{-2} - f_2^{-2}) * DM, \tag{3.3}$$

where D is the dispersion constant set as [17]

$$D = \frac{e^2}{2\pi m_e c} \simeq (4.148808 + -0.000003)10^3 MHz^2 pc^{-1} cm^3 s. \tag{3.4}$$

Here e and m_e are the charge and mass of the electron, respectively, and the uncertainty in D is the result of the uncertainty in those values.

Since DM is an integrated (column) density, it can be used to estimate distances to the pulsar [14]. The accuracy of this distance is highly dependent on the model of the distribution of free electrons in the ISM. For this thesis we used the models YMW [29] and NE2001 [30] for distance estimates to the pulsar. These values are tabulated in Tables 2.3 and 2.4, it is also discussed and presented in Chapter 4. The ATNF database collects the measurement of DM, along with the timing properties of pulsars.

3.4 Results

The correlation of dust and gas along the line of sight is thought to be linear [33]. By comparing E(B-V) and N$_H$, we see that they are indeed correlated for our sample for spiders in SpiderCat. The theoretical correlation has been reported by Predehl and Schmidt [31] and Foight et al. [32]. This correlation implies that the dust and gas volume densities in the Galaxy are correlated. We can see a slight deviation from the linear correlation at higher values.

Figure 3.3 shows the difference between the two dust maps included in SpiderCat. We can see that they agree on the lower values. Where they differ is at the higher values of extinction. At the

Name	E(B-V) SFD	E(g-r) Bayestar	N_H	DM
-	mag	mag	$1/cm$	pc/cm
B1957+20	0.454	0.38	2.87e+21	29.11
J0610-2100	0.073	0.06	8.08e+20	60.67
J2051-0827	0.086	0.11	6.23e+20	20.73
J0023+0923	0.116	0.15	5.01e+20	14.32
J0251+2606	0.131	0.16	9.61e+20	20.22
J0636+5128	0.102	0.09	9.51e+20	11.11
J0952-0607	0.063	0.05	4.38e+20	22.41
J1124-3653	0.108	-	7.77e+20	44.86
J1221-0633	0.026	0.03	2.54e+20	16.43
J1301+0833	0.026	0.01	1.84e+20	13.2
J1311-3430	0.063	-	4.77e+20	37.8
J1317-0157	0.027	0.01	1.73e+20	29.4
J1446-4701	0.153	-	9.7e+20	55.83
J1513-2550	0.124	0.13	7.47e+20	46.88
J1544+4937	0.018	-	1.58e+20	23.22
J1555-2908	0.139	0.13	8.3e+20	75.91
J1627+3219	0.024	0.04	1.52e+20	-
J1630+3550	0.018	0.06	1.19e+20	17.45
J1641+8049	0.043	0.09	3.77e+20	31.09
J1653-0159	0.228	0.25	8.57e+20	-
J1720-0534	0.633	0.58	1.3e+21	-
J1731-1847	0.639	0.72	1.99e+21	106.5
J1745+1017	0.17	0.2	9.89e+20	23.97
J1805+0615	0.241	0.26	1.22e+21	64.88
J1810+1744	0.134	0.13	9.34e+20	39.7
J1928+1245	1.487	1.11	6.09e+21	179.2
J1946-5403	0.05	-	3.51e+20	23.73
J2017-1614	0.074	0.12	4.25e+20	25.44
J2047+1053	0.086	0.1	6.66e+20	34.6
J2052+1219	0.099	0.13	8.76e+20	41.96
J2055+3829	0.698	0.56	4.12e+21	91.83
J2115+5448	1.729	1.05	7.86e+21	77.41
J2214+3000	0.078	0.09	6.12e+20	22.54
J2234+0944	0.116	0.12	7.26e+20	17.83
J2241-5236	0.015	-	1.13e+20	11.41
J2256-1024	0.045	0.01	3.3e+20	13.78
J0336.0+7505	0.243	0.23	1.47e+21	-
J1406+1222	0.026	-	1.9e+20	-
J1408.6-2917	0.055	0.04	3.41e+20	-
J1838.2+3223	0.091	0.11	8.26e+20	-

Table 3.1: The extinction in the optical bands due to dust, the DM due to the free electrons and the column density of hydrogen gas for the black widows in SpiderCat.

higher values, the SFD dust map [23] tells us that there is significantly more extinction along that particular line of sight than the Green et al. dust map [24].

Figures 3.5 and 3.4 show the relation between DM and dust and gas in the Galaxy. What is apparent in both figures is that every system is confined to the upper-left part of the diagrams. In principle, the correlation should be linear, but it does not appear so because of different assumptions in the models of line of sight properties. In common for both gas and dust is that their measurements are pulsar independent, meaning that they are precompiled values of the different coordinates in the sky. DM however, has an explicit dependency on the pulsar, as it is derived from the broadening of the pulse in the radio band. This means that the dust and gas measurement is for a total column value for the entire line of sight, while DM only describes the number of free electrons up to the pulsar but not beyond. For closer pulsars, we expect to see a lower DM than is expected from the dust and gas values for that particular line of sight. This expectation is present in Figures 3.5 and 3.4 which gives plausibility to this intrinsic correlation.

Name	E(B-V) SFD	E(g-r) Bayestar	N_H	DM
-	mag	mag	$1/cm$	pc/cm
J0212+5320	0.188	0.14	1.5e+21	-
J0838-2827	0.166	0.11	1.52e+21	-
J0955-3947	0.207	-	1.25e+21	-
J1023+0038	0.045	0.01	4.06e+20	14.32
J1036-4353	0.141	-	9.99e+20	61.1
J1048+2339	0.043	0.02	2.5e+20	16.65
J1227-4853	0.138	-	1.07e+21	43.42
J1242-4712	0.097	-	8.58e+20	-
J1302-3258	0.074	-	5.55e+20	26.19
J1306-4035	0.091	-	7.1e+20	35
J1417-4402	0.118	-	7.16e+20	55
J1431-4715	0.167	-	1.11e+21	59.35
J1622-0315	0.245	0.25	9.57e+20	21.41
J1628-3205	0.392	-	1.61e+21	42.15
J1723-2837	1.262	1.45	3.72e+21	19.69
J1803-6707	0.066	-	5.75e+20	38.38
J1816+4510	0.04	0.05	3.72e+20	38.89
J1908+2105	0.839	0.71	3.2e+21	61.91
J1910-5320	0.07	-	5.22e+20	-
J1957+2516	2.03	1.24	7.11e+21	44.14
J2039-5617	0.058	-	5.57e+20	24.57
J2055+1545	0.086	0.08	6.63e+20	-
J2129-0429	0.039	0.01	3.24e+20	16.88
J2215+5135	0.351	0.24	2.79e+21	69.2
J2333-5526	0.014	-	1.07e+20	-
J2339-0533	0.033	0.01	2.95e+20	8.717
J0407.7-5702	0.015	-	1.08e+20	-
J0427.9-6704	0.044	-	3.51e+20	-
J0523-2529	0.027	0.04	1.48e+20	-
J0935.3+0901	0.04	0.06	3.55e+20	-
J0940.3-7610	0.286	-	9.54e+20	-
J1544-1128	0.218	0.19	1.25e+21	-
J1646.5-4406	7.908	-	1.41e+22	-
J1702.7-5655	0.184	-	1.26e+21	-
J2054.2+6904	0.453	0.42	1.94e+21	-
J0846.0+2820	0.056	0.06	4.54e+20	-

Table 3.2: The extinction in the optical bands due to dust, the DM due to the free electrons and the column density of hydrogen gas for the redbacks in SpiderCat.

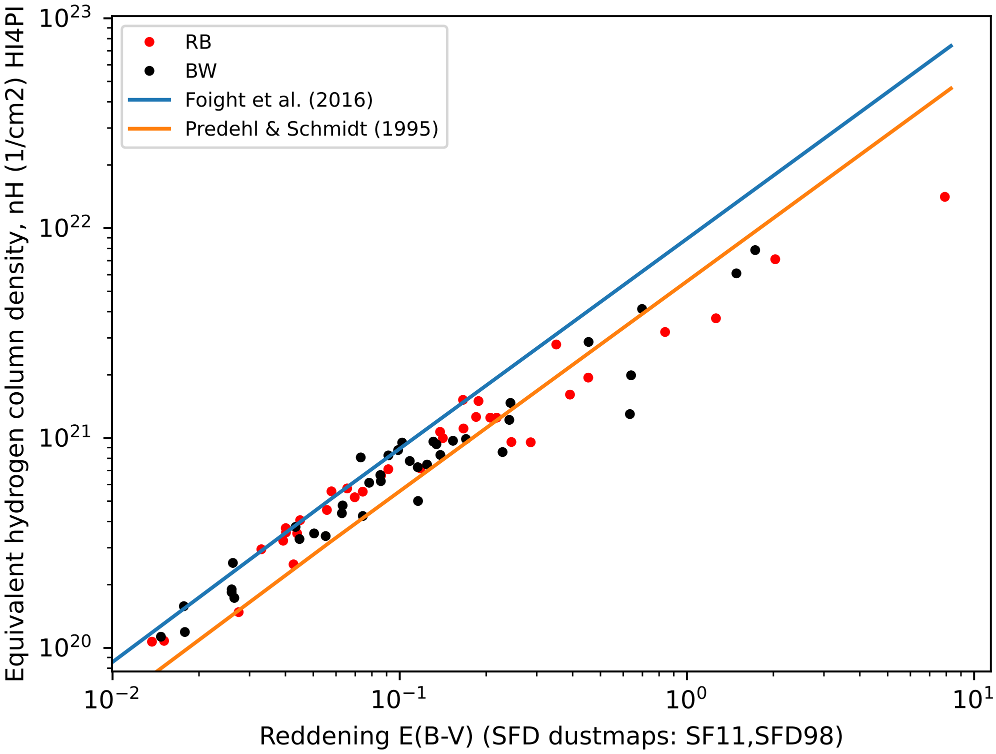

Figure 3.2: N_H vs E(b-v). The linear line by Predehl is expressed by the formula $N_H = 1.8 * 10^{21} E(B-V) R_v$ [31] Here we use the value 3.1 for R_v [25]. The line by Foight follows $N_H = 2.87 * 10^{21} E(B-V) R_v$ [32].

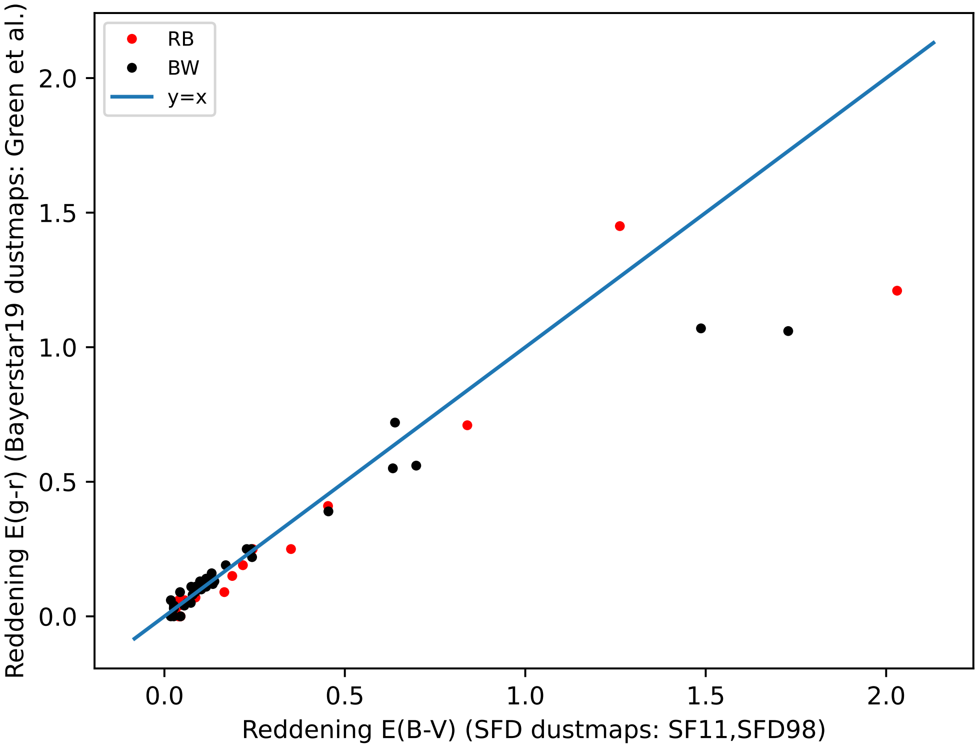

Figure 3.3: A comparison of the two dust maps Bayestar [24] and SFD [23]. If the two different models agree we would expect them to follow the line x=y.

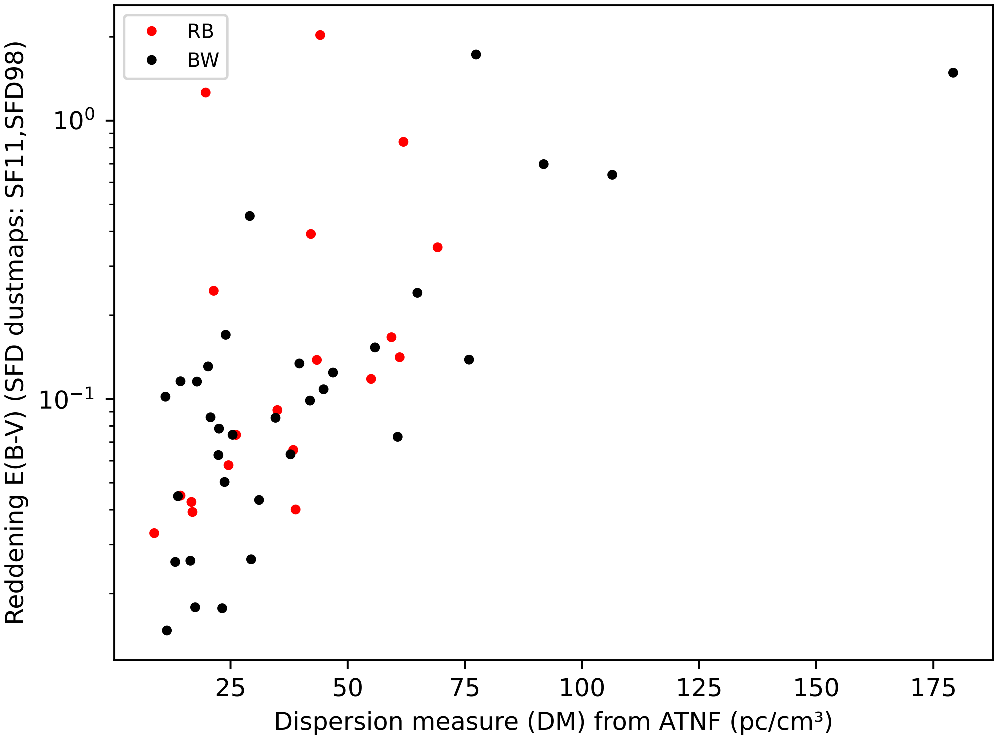

Figure 3.4: DM [11] from the free electrons against the reddening from dust particles using the SFD [23] dustmap. E(B-V) is plotted in a logarithmic scale.

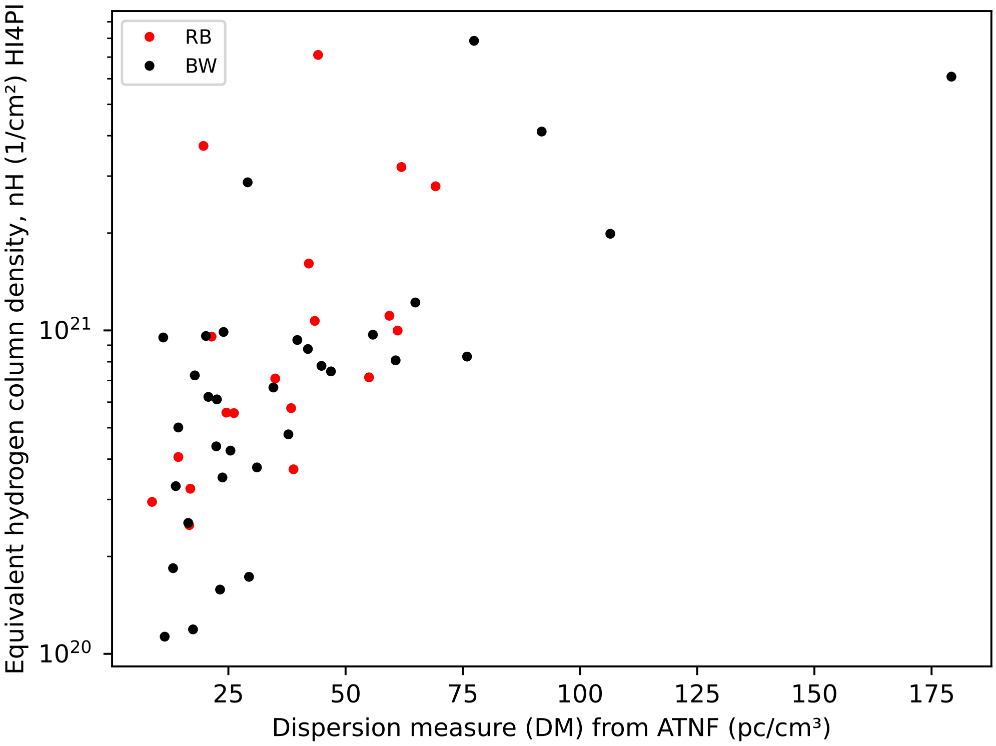

Figure 3.5: DM [11] from the free electrons hydrogen gas number denisty using the HI4PI [22] database. N_H is plotted in a logarithmic scale.

Chapter 4

Astrometry

Astrometry is the branch of astronomy devoted to determining the exact positions and movements of stars and celestial objects. As part of SpiderCat, we review astrometric concepts and measurable quantities and compile a list of spiders' astrometric properties.

4.1 Parallax

Trigonometric parallax (or 'parallax' hereafter) is the apparent movement of a star on the plane of the sky due to the orbit of the Earth around the Sun. Looking at a closer star, we can see an apparent movement with respect to the background objects throughout the year. Parallax is the star's maximum angular movement through the year on the sky's plane due to the Earth's orbit.

Parallax is also tightly bound with distance. If we know both the parallax and the distance between the Sun and the Earth, the distance to the star can be derived using fundamental trigonometry. Figure 4.1 shows both the trigonometry of the system and the view from an observer on Earth. The distance is expressed as $d = 1AU/tan(p_x)$, where 1 AU $\simeq$ 1.510^8 km is the mean distance between the Earth and the Sun. The methodology of using parallax to infer the distance of stars is so standard that it gave birth to a new unit of distance in astronomy: one parsec (pc) is defined as the distance to a star with a parallax of 1 arcsec. Using the units of parsec and approximating for small parallaxes (in radians) $tan(p_x) = p_x$, the relation is simplified to $d = 1/p_x$. In this relation, d is in units of parsec, and p_x is in arcseconds.

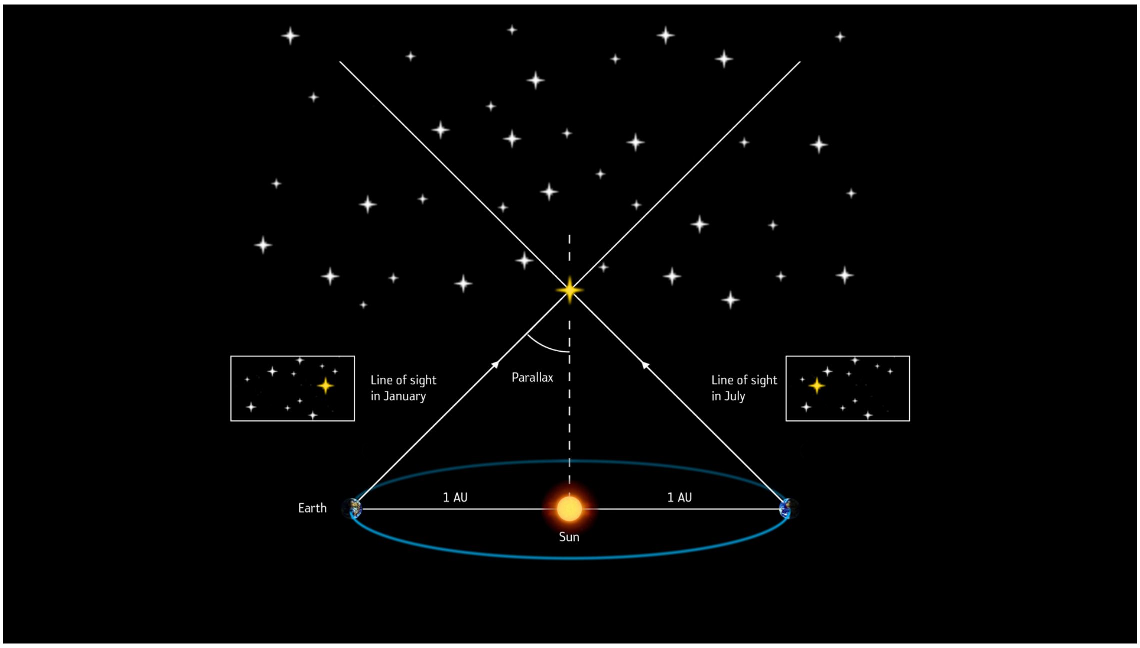

Figure 4.1: An illustration of parallax. Credit: ESA.

This method has limitations, as it becomes less accurate for more distant stars because the fractional uncertainty becomes large. The distance and the parallax are inversely related, so there will be significant uncertainties for more distant stars. It is also a slow way to do a measurement. By its nature, you need to make measurements of the same star through a whole year to measure the parallax.

4.2 Proper motion

Proper motion is the motion of a celestial object on the plane of the sky. Stars are not stationary objects and move around in the Galaxy. This movement on the plane of the sky is slow but noticeable. The way to measure proper motion is based on determining the precise position of a star, monitoring its change in position, and removing the annual parallax. Proper motion was suspected by the early Greek astronomers in 400 BC. In 1718, the astronomer Edmund Halley noticed that Sirius was half a degree away from the positions charted by the ancient Greeks [34]. The further a star is, the faster it will have to travel through space in order to have an equal proper motion to that of a closer star. The highest proper motion star is Bernard's star, with a proper motion of 10.3 arcseconds in a year [34]. At this rate, it would take 180 years to travel the moon's diameter, which covers half a degree of the night sky.

When dealing with proper motion in the coordinates of Right Ascension (RA) and Declination (DEC), a specific correction is made due to the spherical geometry of the plane of the sky. To understand this correction, one must consider the RA and DEC coordinate system. RA is analogous to longitude but measured in time units (hours, minutes, and seconds), where 24 hours completes a full circle of 360 degrees. It measures the east-west position of objects on the celestial sphere. DEC is analogous to latitude and is measured in degrees north or south of the celestial equator. The celestial sphere's lines of RA converge at the poles, similar to the meridians of longitude on Earth. This means that a constant angular speed in RA does not correspond to a constant linear speed across the sky. To correct this, the proper motion in RA must be multiplied by the cosine of the DEC. This factor accounts for the convergence of the lines of RA at the poles. The actual formula for the corrected proper motion in RA, denoted as μ_{RA}, is:

$$\mu_{RA} = \mu_{RA,raw} * \cos(DEC), \tag{4.1}$$

where $\mu_{RA,raw}$ is the raw measurement of the proper motion in RA.

4.3 Gaia DR3

The Gaia mission, launched by the European Space Agency, is the state of the art in astronomy. The mission for Gaia is to map one billion stars, approximately 1% of the total population in our Galaxy. Gaia, orbiting the second Lagrange point (L2), creates a precise and comprehensive three-dimensional map of the Galaxy [35]. With data releases, such as the early third data release (EDR3) and the complete third release (DR3), Gaia facilitated a more advanced understanding of the astronomic and photometric (in the optical band) properties of our Galaxy[36, 37]. Moreover, Gaia's mission extends beyond the mapping of stars. It provides significant insights into the physical properties of thousands of exoplanets, asteroids within our Solar system, and numerous distant galaxies. Additionally, Gaia's data contribute to the testing of General Relativity and other theories of gravity. By offering this wealth of information, Gaia is a cornerstone mission for astrophysics [36].

Gaia is an optical telescope that measures and maps all the light sources in the optical band. Given that pulsars emit pulses in the radio band, Gaia has not detected these. However, when knowing the position of a pulsar or a candidate, we can look for what is known as a counterpart in the optical band. A counterpart is a source detected in another band in the same position as the system we are interested in. In the case of spiders, the light from the companion stars dominates in the optical band.

We can calculate the source density per unit angular area as in Section 2.3, but now we have a significantly larger population of stars to account for. There are 1 billion optical sources, and this results in an average separation of 26.1 arcseconds. To confidently conclude that the counterpart is for the same system, we must use a smaller radius for the search. Or to be more precise a search width. The positional search in Gaia is based on an uncertainty in both the RA and the DEC. Consequently, the search area becomes a square with a selected width. The chosen width was 4 arcseconds. This is well below the average separation of sources given 1 billion sources on a celestial sphere. This leads to a chance of a spurious match being 12%.

The vast data in the EDR3 and the complete GDR3 is made accessible through the Python package ASTROQUERY. ASTROQUERY.GAIA is a powerful Python module designed as part of the ASTROQUERY library, which provides tools to query astronomical web forms and databases. The Gaia submodule specifically facilitates access to the data released by the European Space Agency's Gaia mission, which includes extensive astrometric and photometric data. Through simple Python commands, we retrieved data about positions, radial velocities, magnitudes, and parallaxes directly from the Gaia archive.

4.4 Distances

Stellar distances are a fundamental part of astrophysics. There are several techniques for determining a stellar distance. As discussed in Section 4.1, parallax is one such way, but it works poorly for distant and faint stars with a high fractional parallax uncertainty. Other techniques include Doppler shift, standard candles, extinction, DM and other ISM estimates. Most of these techniques rely on assumptions, making them educated guesses. After the EDR3, Bailer-Jones et al. [38] looked at the 1.47 billion parallaxes and estimated distances. For the more distant stars, they made two models for the distances. The first was a geometric model including the parallax and the position. The position was included in the model to account for the stellar distribution in the Galaxy. In this model, stars close to the Galactic disk are, with a higher probability, farther away than those above or below the Galactic disk. The second model included photometric properties. In this model, they also accounted for a star's color and magnitude. With previous knowledge of the color and intrinsic luminosity of many types of stars, Bailer-Jones used the change in color due to extinction and the apparent luminosity as a secondary distance measurement and got even more accurate estimates. The two models from Bailer-Jones indicates the complexity of the problem. Highlighting that making more assumptions and accounting for more factors we get better estimates.

Name –	RA deg	err as	DEC deg	err as	Px mas	err mas	PmRA mas/yr	err mas/yr	PmDEC mas/yr	err mas/yr
B1957+20	299.903	0.38	20.8044	0.38	0.7	0.53	-1.82	0.5	-5.01	0.53
J1311-3430	197.941	1.1	-34.5084	0.63	1.93	0.97	-6.13	1.6	-5.14	0.68
J1555-2908	238.919	1	-29.1412	0.57	-	-	-	-	-	-
J1653-0159	253.409	0.63	-1.97692	0.35	1.77	0.78	-17.3	0.95	-3.24	0.72
J1731-1847	262.823	0.63	-18.7925	0.44	-	-	0.707	0.72	-3.18	0.93
J1810+1744	272.655	0.38	17.7437	0.44	0.648	0.54	7.54	0.45	-4.19	0.51
J1928+1245	292.189	0.11	12.7648	0.13	-	-	0.148	0.17	-0.35	0.16
J2055+3829	313.793	1.8	38.4915	2.6	-	-	-	-	-	-
J0336.0+7505	54.0424	1.8	75.0548	1	-	-	-0.852	1.6	-0.746	2.1
J1406+1222	211.734	4.4	12.3787	3.4	-	-	-	-	-	-
J1408.6-2917	212.112	2.4	-29.3726	1	-	-	-	-	-	-
J1838.2+3223	279.57	1.6	32.4032	1.1	-	-	1.61	1.6	-4.89	2

Table 4.1: The astrometric properties of the black widows with an optical counterpart in Gaia DR3.

Two other papers that also have done extensive distance estimates, YMW16 [29] and NE2001 [30], are both accessible through the python package PYGEDM [39]. These distance estimates are estimates based on the DM from the pulsars. Consequently, both methods rely on a model of free electron distribution in the Galaxy. The YMW16 model, named after the authors: Yao, Manchester and Wang, assumes a thick disk Galactic model (scale height 1.6 kpc) with a non-homogeneous electron number density model, with the exceptions of "Fermi bubbles" [29]. The model has 96 parameters, with 64 fixed and 32 fitted. They compared their results to those of 189 pulsars with independently determined distances to validate their model. What separates YMW16 from NE2001 includes the 15 years in publication, in which discoveries and updated models have been discovered. Quantitatively, YMW16 claims that "the YMW16 mid-plane density is about one-third the NE2001 value and the scale height is about 70% larger than the NE2001 value [29]." To determine the distance they utilize the models and integrate the free electron number density in their model until it fits with the measured DM, how distance is correlated to distance is explained in Section 3.3. PYGEDM is a tool developed to access distance estimated based on the two models NE2001 and YMW16. The package allows for easy calculation of both distance and scattering measures based on user-supplied Galactic coordinates and DM.

4.5 Results

The proper motion measurements of the spiders cataloged in the SpiderCat dataset predominantly fall within a range of -20 to 20 milliarcseconds per year (mas/year) in both RA and DEC. This observed range encompasses the expected values for such celestial objects, indicating a relatively consistent pattern among most cataloged spiders.

Within these ranges, a marginal disparity between black widows and redbacks emerges. Notably, redback pulsars exhibit higher proper motions than the black widows. In Figure 4.2, all six black widows show a significantly lower proper motion in DEC than the redbacks. In total, the redbacks seem to be more scattered in both RA and DEC (except black widow J1653-0159). This discrepancy is also apparent in Figure 4.3, where the total proper motion is plotted against the parallax. We see that the spiders with the highest angular movement are redbacks. This could be explained by the evolutionary process of the pulsar binary.

In Figure 4.4, we observe the distance estimates derived from the DM plotted against the DM values. If the YMW model's distance estimates were solely dependent on DM, we would anticipate a clear functional relationship and strong correlation between these two variables. However, as outlined in the YMW model documentation [29] and evident in Figure 4.4, this is not the case. Despite this, Figure 4.4 reveals a somewhat scattered yet linear relationship between DM and distance. The non isotropic distribution of free electrons in our Galaxy accounts for deviations from the expected distance-DM relationship for certain lines of sight. The figure ultimately supports the reasonable conclusion that more distant spiders exhibit larger dispersion measures. This is an expected result as the ISM is present throughout our entire Galaxy: the further away from Earth

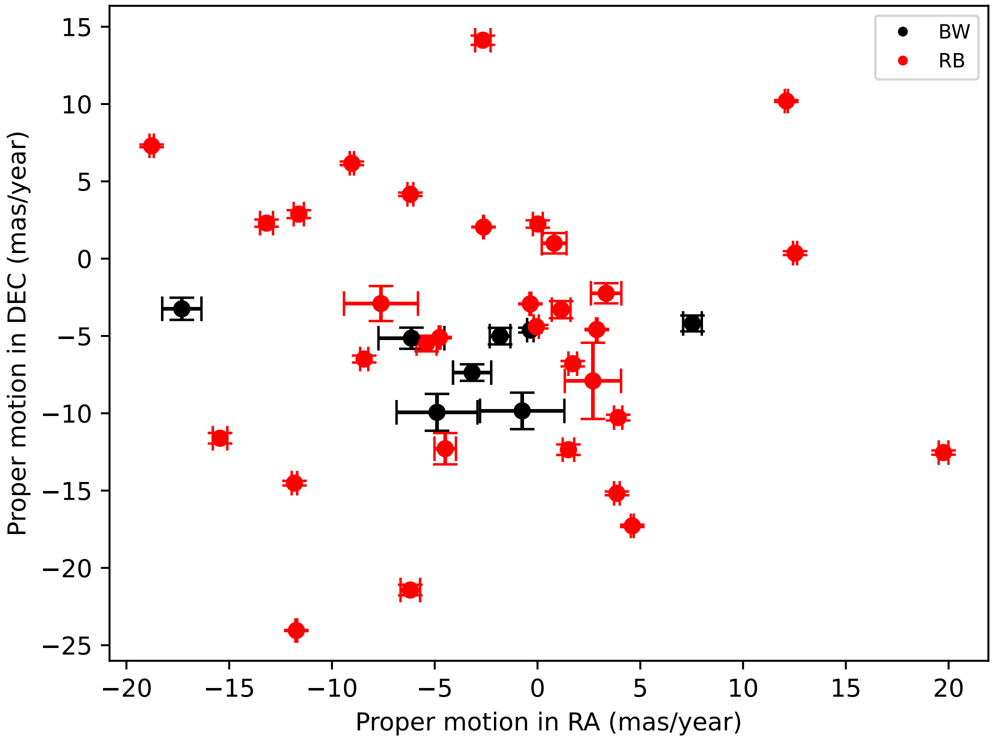

Figure 4.2: Proper motions in RA and DEC as found in GDR3 [37].

a spider is, the higher is the integrated electron density in the line of sight.

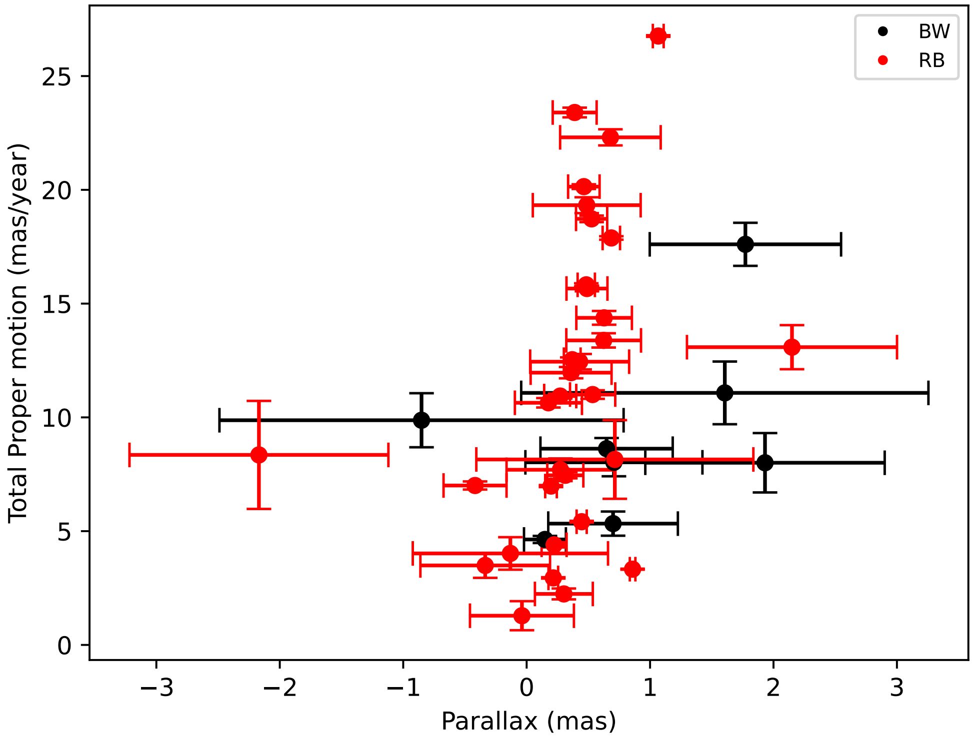

Figure 4.3: Total proper motion plotted against the parallax.

Name	RA	err	DEC	err	Px	err	PmRA	err	PmDEC	err
–	deg	as	deg	as	mas	mas	mas/yr	mas/yr	mas/yr	mas/yr
J0212+5320	33.0436	0.016	53.3608	0.017	0.858445	0.023	-2.62665	0.023	2.04433	0.021
J0838-2827	129.71	0.21	-28.4658	0.27	0.429425	0.4	1.504	0.28	-12.3555	0.34
J0955-3947	148.866	0.084	-39.7979	0.099	0.271978	0.13	-9.03195	0.1	6.16707	0.12
J1023+0038	155.949	0.058	0.644647	0.055	0.686171	0.071	4.6099	0.071	-17.281	0.077
J1036-4353	159.126	0.21	-43.8858	0.24	0.3603	0.33	-11.6133	0.25	2.8793	0.26
J1048+2339	162.181	0.31	23.6648	0.38	0.486926	0.44	-15.4452	0.35	-11.6146	0.34
J1227-4853	186.995	0.097	-48.8952	0.061	0.463501	0.13	-18.7724	0.11	7.29737	0.088
J1306-4035	196.734	0.13	-40.5898	0.11	0.313287	0.15	-6.18544	0.14	4.16104	0.11
J1417-4402	214.377	0.04	-44.0493	0.033	0.197373	0.047	-4.76375	0.043	-5.10322	0.047
J1431-4715	217.936	0.082	-47.2577	0.11	0.526437	0.13	-11.8247	0.13	-14.5189	0.15
J1622-0315	245.748	0.25	-3.26035	0.19	0.623945	0.3	-13.1843	0.32	2.29789	0.23
J1628-3205	247.029	0.34	-32.097	0.24	0.678687	0.41	-6.18791	0.48	-21.4313	0.34
J1723-2837	260.847	0.036	-28.6327	0.025	1.06634	0.044	-11.7338	0.044	-24.0497	0.034
J1803-6707	270.768	0.15	-67.1267	0.19	-	-	0.176439	0.27	-8.43157	0.2
J1816+4510	274.15	0.094	45.1761	0.096	0.222498	0.1	-0.0586163	0.12	-4.39951	0.12
J1908+2105	287.239	0.82	21.0839	1.8	-	-	-2.16891	1	2.69529	1.4
J1910-5320	287.705	0.18	-53.3492	0.18	-	-	-0.417998	0.26	1.71393	0.21
J1957+2516	299.394	0.36	25.2672	0.66	2.14979	0.85	-4.49069	0.52	-12.2909	1
J2039-5617	309.896	0.12	-56.2859	0.1	0.48869	0.17	3.86106	0.14	-15.1797	0.12
J2055+1545	313.949	0.68	15.7559	0.49	-	-	-0.131655	0.79	3.33887	0.74
J2129-0429	322.438	0.06	-4.48523	0.055	0.483132	0.07	12.1043	0.074	10.194	0.06
J2215+5135	333.886	0.18	51.5935	0.2	0.301575	0.23	0.0143901	0.24	2.2403	0.24
J2333-5526	353.317	0.34	-55.4392	0.39	-	-	-0.335637	0.53	1.14884	0.46
J2339-0533	354.911	0.16	-5.55146	0.14	0.534644	0.18	3.92366	0.2	-10.2796	0.19
J0407.7-5702	61.8822	0.42	-57.007	0.5	-	-	-0.038033	0.42	0.808894	0.6
J0427.9-6704	66.9569	0.072	-67.0764	0.07	0.369446	0.068	12.5297	0.1	0.358961	0.12
J0523-2529	80.8205	0.029	-25.4603	0.031	0.445812	0.041	2.88141	0.038	-4.58396	0.041
J0935.3+0901	143.836	1.5	9.00997	1.1	-	-	0.714495	1.1	-7.61581	1.8
J0940.3-7610	145.099	0.22	-76.1667	0.2	0.627672	0.23	-2.65933	0.38	14.1264	0.3
J1544-1128	236.164	0.18	-11.468	0.11	0.389214	0.18	19.7542	0.24	-12.5413	0.14
J2054.2+6904	313.496	0.39	69.0888	0.46	-	-	0.273963	0.44	-5.39696	0.49
J0846.0+2820	131.591	0.032	28.1447	0.019	0.215959	0.039	-0.349818	0.042	-2.92427	0.03

Table 4.2: The astrometric properties of the redbacks with an optical counterpart in Gaia DR3.

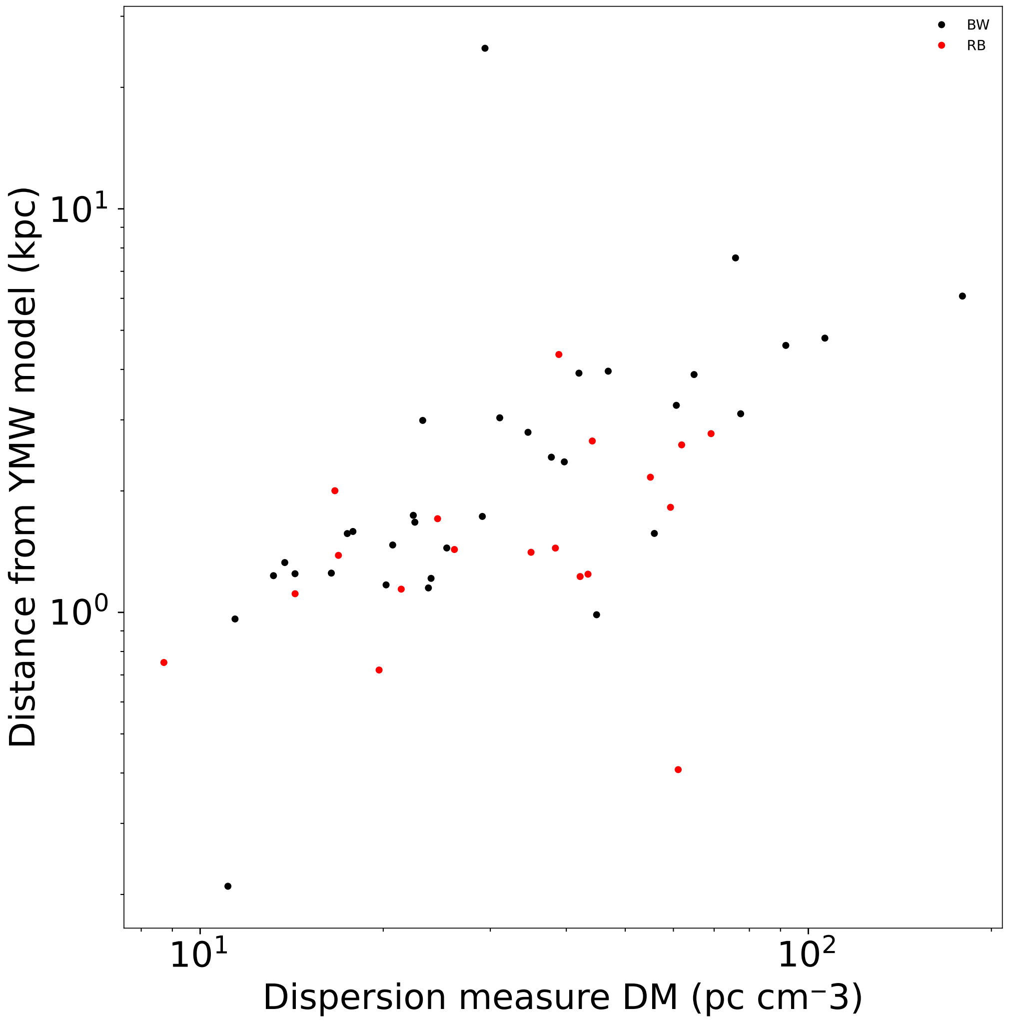

Figure 4.4: The estimated distances for the YMW model [29] plotted against the DM from ATNF [11].

Chapter 5

Photometry

5.1 Magnitudes and color index

Photometry is the study of the brightness and intensity of astrophysical sources, specifically looking at the number of photons and the energy they carry. Using a CCD detector, we can determine the number of photons and their energy. In addition to a CCD detector, a bandpass filter is used to isolate a specific part of the EM spectrum.

The brightness of celestial objects is measured using an inverted magnitude scale. Lower magnitude values signify brighter objects, and higher values denote dimmer ones. Magnitude is a dimensionless value and is specified for each bandpass. Magnitudes originated in ancient Greece, where astronomers categorized stars into six magnitudes. The first magnitude was placed on the first stars to appear at dusk, and the sixth magnitude was for stars just visible to the naked eye. Based on these two reference points with the brightest and dimmest stars in the night sky we have with modern observations, determined that the flux ratio between magnitude 6 and 1 is approximately 1% [27]. Thus,

$$m_1 - m_2 = 5 = -xlog_{10}(F_1/F_2) = -xlog_{10}(100) = -2x. \tag{5.1}$$

The negative sign is added to ensure the brighter source has a lower numerical value. Expanding this to find the magnitude of any source means introducing a reference source and comparing the flux from this source. So the apparent magnitude as seen from Earth for an object is given by

$$m_1 - m_{ref} = -2.5log_{10}(F_1/F_{ref}). \tag{5.2}$$

The absolute magnitude is how bright the object would appear if the source was ten pc away from the observer. Most stars' apparent magnitude is higher than their absolute magnitude because they are excede this 10 pc distance.

Once the magnitudes of an astronomical object have been measured across various bands, one can calculate its color index. The color index is a quantitative measure that reflects the object's spectral energy distribution. It is derived by subtracting the magnitude measured in one band from another. The color index serves as a valuable indicator of the object's color, as well as its temperature and spectral type. Hotter stars have lower color indices and appear bluer, whereas colder stars appear more red. This correlation between color index and temperature follows the principles of blackbody radiation, where hotter bodies emit more radiation at shorter, bluer wavelengths. Additionally, the color index aids in identifying a star's spectral type. Flux is the amount of energy originating from a luminous source that arrives at the observer per area and time. Flux is used to quantify the intensity of the light arriving.

5.2 Optical

Pulsars are very weak optical sources. Even after we suspected there to be a pulsar in the Crab Nebula, it took some time before Cocke et al. [40] found pulsations in the optical band in 1969, and subsequently, it took almost a decade for the second pulsar to be discovered in the optical band by Wallace [41].

The optical light observed in spider systems predominantly originates from the companion star as blackbody radiation. This radiation can be affected by the NS if it heats the companion star, typically causing the side of the companion facing the NS to become warmer, while the opposite side remains cooler. However, efficient heat distribution through convection within the companion can mitigate this effect. Additionally, the presence of an inter-binary shock boundary that curves around the companion might lead to heating from synchrotron radiation on multiple sides.

The Panoramic Survey Telescope and Rapid Response System (Pan-STARRS)[26] is a telescope project primarily designed for observing the sky in wide-field imaging. Located at Haleakalā Observatory in Hawaii, it was built to survey the sky for asteroids that could potentially threaten Earth and to observe transient phenomena like supernovae. Pan-STARRS uses a 1.8-meter telescope equipped with a 1.4 Gigapixel camera. The Pan-STARRS maps the sky north of DEC -30°. The detection limit for the apparent magnitude is 24 across the optical bands [42]. Saturation of the CCD happens around 12-14 mag depending on filter and band and imposes a limit on magnitude. The Pan-STARRS's field of view is 7 square degrees, using g, r, i, z and y filters.

The mean wavelength for the different bands utilized in Pan-STARRS is 4866Å, 6215Å, 7545Å, 8679Å and 9633Å for the green (g), red (r), near-infrared (i), z and y bandpasses respectfully [43]. As we see in Figure 5.1, these have different widths, and in combination, they cover the entire optical and some infrared range [44].

We searched for counterparts in Pan-STARRS using a radius of 10 arcseconds. In addition to the query for optical counterparts in Pan-STARRS, we have searched for optical counterparts in the Gaia DR3 (see Chapter 4).

5.3 X-ray

The X-ray radiation from a spider system is mainly produced by the interaction between the NS and the companion. In spiders, an inter-binary shock can occur when the pulsar wind from the NS and stellar wind from the companion collide, creating a shock. At this boundary, the magnetic field intensifies, potentially accelerating particles like electrons to relativistic speeds. These electrons may emit synchrotron radiation, observable in the X-ray or γ-ray bands, depending on the magnetic field strength [46]. The emission is not isotropic, often resulting in a double-peaked flux pattern across the binary's orbit due to the alignment of the shock boundary with the line of sight. There is also a base level for the flux in these cases when the border for the inter-binary shock is misaligned with the line of sight. When the binary orbit is compact, we will observe a stronger interaction between the companions and thus an increase in the X-ray radiation from the intra-binary shock [46]. X-ray emissions may also arise from heating the NS's polar caps. Strong magnetic fields channel charged particles to these caps, heating them to millions of degrees and causing them to emit blackbody radiation in the X-ray band.

The NASA Swift mission [47], launched in November 2004, is designed to detect and study gamma-ray bursts (GRBs), the universe's most luminous and energetic phenomena. Swift's multi-wavelength observational capabilities, integrating a Burst Alert Telescope, an X-ray telescope (XRT), and an Ultraviolet/Optical Telescope, allow for immediate and comprehensive follow-up observations of GRBs and their afterglows [47].

The XRT on the Swift mission is a crucial instrument for investigating the afterglow phase of GRBs and other astronomical phenomena. Equipped with a grazing incidence Wolter I telescope design, the XRT operates in the 0.2 to 10 keV energy range, providing both imaging and spectroscopic

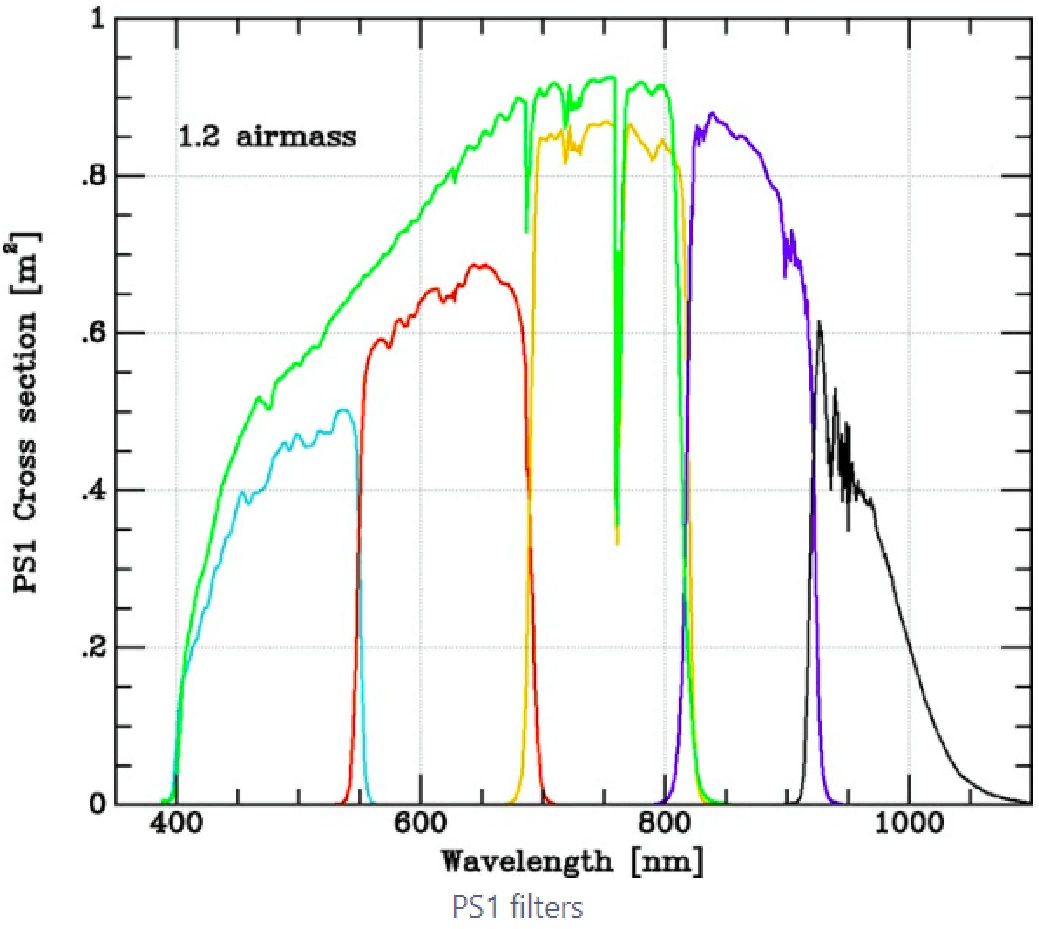

Figure 5.1: Figure from Tonry et al. 2012 [45]: The Pan-STARRS capture cross-section in $m^2/e/photon$ to produce a detected e for an incident photon for the six Pan-STARRS bandpasses, grizy for a standard airmass of 1.2. The overlapping band is ω_{P1} [45].

data. The Swift XRT point source (2SXPS) catalog is a point source catalog built from all Swift XRT photon counting mode data of at least 50 s in duration gathered between January 1st, 2005, and August 1st, 2018. It contains position, fluxes, spectral details, variability information, count rate, and a flag indicating the reliability of the detection for 206335 objects [48]. One of the measurements obtained from the X-ray counterparts was the count rate. The count rate is, in this case, divided into four different bands. The first one, labeled CR0, is the total count rate from 0.3 to 10 keV. CR1 is the soft band of 0.3-1keV. Medium CR2 is in the band from 1-2 keV. The hard band is from 2-10keV. In addition, there was also an addition of 1 sigma uncertainty in both positive and negative directions. The 1 σ uncertainties were labeled with a capital E for the positive and a small e for the negative. For our uncertainty estimates we used the average of the positive and negative 1 σ uncertainty. The source detection of the count rate was done in each of these bands independently, and the results were combined in the 2SXPS catalog.

5.4 Results

Figure 5.2 shows the photometric results from the Gaia DR3, as discussed in Chapter 4.2. The color-magnitude diagram (CMD) shows that redbacks are, on average, brighter than black widows in the g band because their companions are typically larger and hotter than those of black widows. We also find an outlier, J1816+4510. J1816 appears so blue because its companion is unusually hot at 16000K, a suspected proto-white dwarf [49].

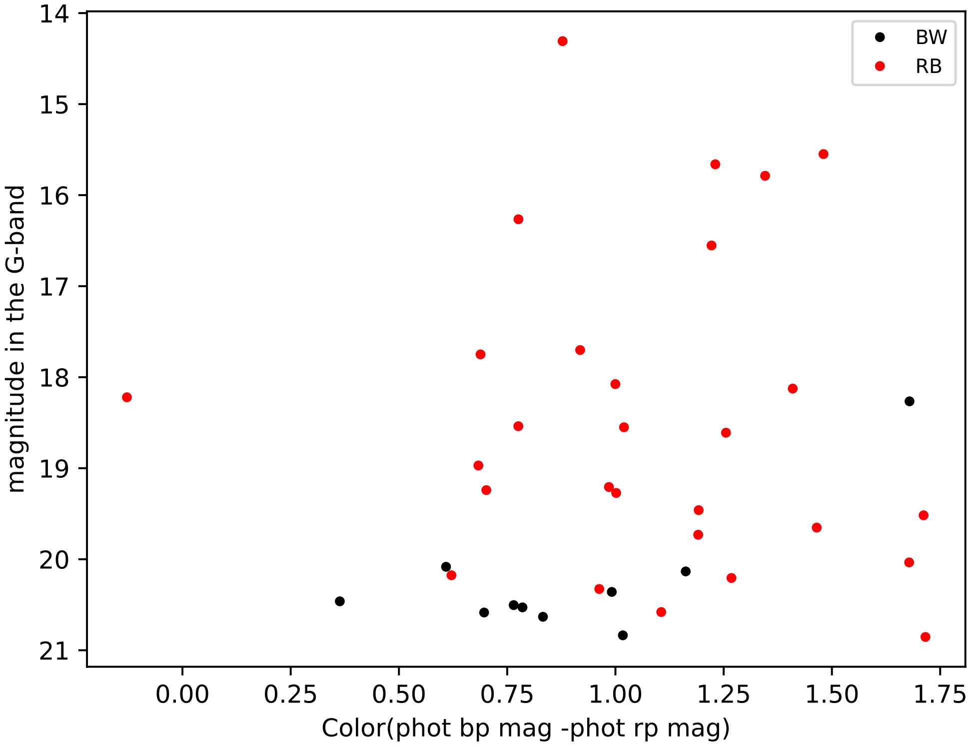

Figure 5.2: A color-magnitude diagram (CMD) where the BP-RP color is plotted against magnitude in the G band. From the optical counterparts found in Gaia DR3.

Also, in the Pan-STARRS CMD, Figure 5.3, we see the presence of J1816 as the leftmost point, reaffirming its significance. A second observation is that the black widows are dimmer in the optical band. There are also fewer black widow optical counterparts. This is coherent with the lower magnitude limit at 21 magnitudes for GDR3. We conclude that most optical counterparts for black widows are not detected in Pan-STARRS or Gaia because they are fainter than the detection limit.

Another point to note is that these values are fixed for the optical surveys by Gaia and Pan-STARRS, especially for black widows. This is problematic because the black widows typically have a high variability in their optical magnitude. This magnitude fluctuation is due to the orbital rotation of the companion. The black widow companion is much smaller and less hot than the redback companion, so they have a much higher ratio between their irradiated hot side and the cold side. The side facing the pulsar is heated by the pulsar winds. When this side is facing the observer, we observe blackbody radiation from a much hotter companion. This will in turn result in a brighter companion and a lower numerical magnitude.

When looking at Figure 5.4, we can see that there are three redbacks that have the highest unabsorbed fluxes. These are J1023, J1227, and J1544, all of which are classified as transitional MSPs. Given their high X-ray fluxes, it is likely that Swift observed them during their luminous disk state. Transitional MSPs are a special subclass of MSPs that switch between two different states: a radio pulsar state and a low-mass X-ray binary (LMXB) state. In the radio pulsar state, the MSP emits predominantly in the radio wavelengths and is powered by the rotation of the NS. However, in the LMXB state, the MSP accretes matter from its companion star, forming an accretion disk that emits strongly in X-rays. The high X-ray fluxes observed in these transitional MSPs are indicative of the LMXB state. During this state, the accretion of material from the companion star onto the NS releases a significant amount of energy, which is converted into X-rays. This process involves the formation of an accretion disk around the NS, where matter spirals

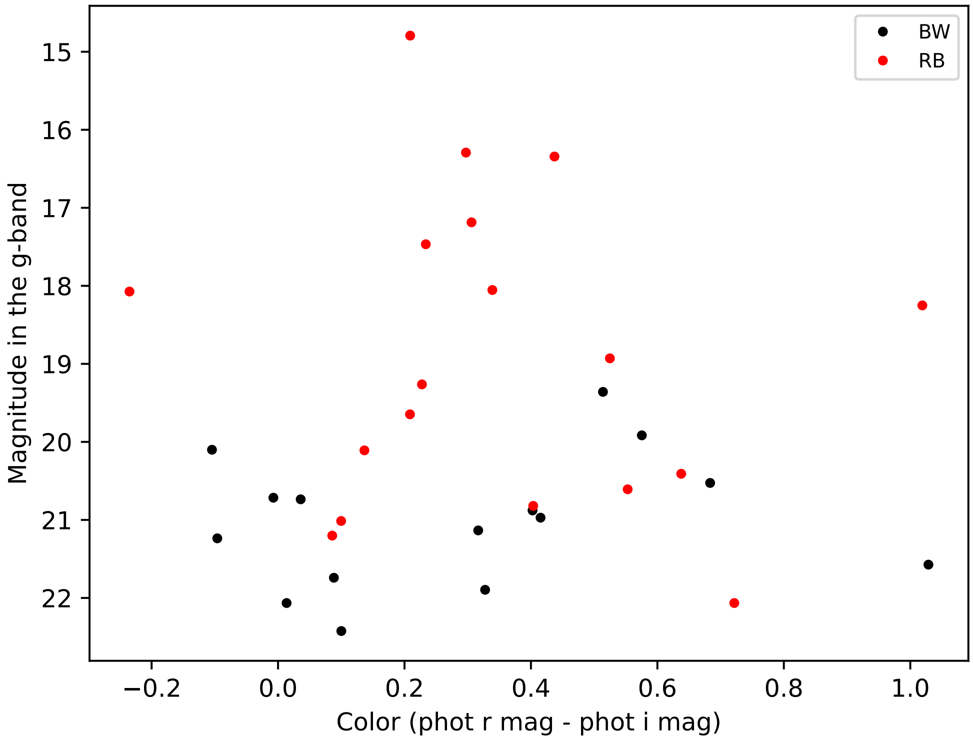

Figure 5.3: Color magnitude diagram, where the r-i color i plotted against magnitude in the g band. These results are based on the Pan-STARRS in the optical band.

inwards and heats up to temperatures of millions of degrees, emitting X-rays in the process. The transition between these states can be triggered by changes in the mass transfer rate from the companion star or alterations in the magnetic field configuration of the MSP.

Name -	d as	CR0 (c/s)	err (c/s)	CR3 (c/s)	err (c/s)	$F_{U0}/10^{-12}$ erg/s/cm^2	10^{-12}err $erg/s/cm^2$	UFL0/err UFL0/err
J0212+5320	0.48	0.0247	0.00279	0.0127	0.00199	1.7	0.1924	8.8
J1023+0038	0.33	0.307	0.00123	0.0977	0.000705	13.3	0.05346	248.8
J1048+2339	1.23	0.00205	0.000684	0.0014	0.000534	0.0909	0.03039	3.0
J1227-4853	1.89	0.149	0.00155	0.0597	0.00097	8.18	0.08507	96.2
J1306-40	2.2	0.0214	0.00138	0.00797	0.000748	1.19	0.07674	15.5
J1628-3205	7.18	0.0014	0.000515	0.000794	0.000337	0.104	0.03816	2.7
J1723-2837	1.81	0.0338	0.00113	0.018	0.000806	2.55	0.08506	30.0
J2039-5618	1.36	0.00193	0.000224	0.000565	0.000124	0.0902	0.01047	8.6
J2129-0429	1.67	0.00549	0.000612	0.00244	0.000404	0.336	0.0375	9.0
J2215+5135	4.61	0.00272	0.00044	0.00132	0.000296	0.211	0.03415	6.2
J2339-0533	0.89	0.00532	0.000463	0.00178	0.000264	0.259	0.02254	11.5
J0427.9-6704	0.24	0.0163	0.00154	0.0135	0.00138	2.22	0.2097	10.6
J0523-2529	1.77	0.00637	0.000661	0.00188	0.000365	0.294	0.03057	9.6
J0838.8-2829	3.04	0.0007	0.000441	0.000341	0.000291	0.0389	0.02452	1.6
J0935.3+0901	2.8	0.00614	0.00173	0.000622	0.000632	0.307	0.08633	3.6
J0940.3-7610	1.3	0.0068	0.00212	0.00379	0.00153	0.51	0.1592	3.2
J0954.8-3948	0.49	0.00449	0.000916	0.00246	0.000657	0.345	0.07049	4.9
J1544-1128	2.11	0.0888	0.00113	0.0343	0.000711	4.84	0.06147	78.7
J2054.2+6904	1.35	0.00229	0.000445	0.00147	0.000347	0.144	0.02804	5.1
J2333.1-5527	6.07	0.00115	0.000637	0.000554	0.000415	0.0718	0.03962	1.8
J1417.5-4402	1.93	0.0188	0.00126	0.00676	0.000739	1.07	0.07157	15.0

Table 5.1: Swift results for Redbacks in table format.

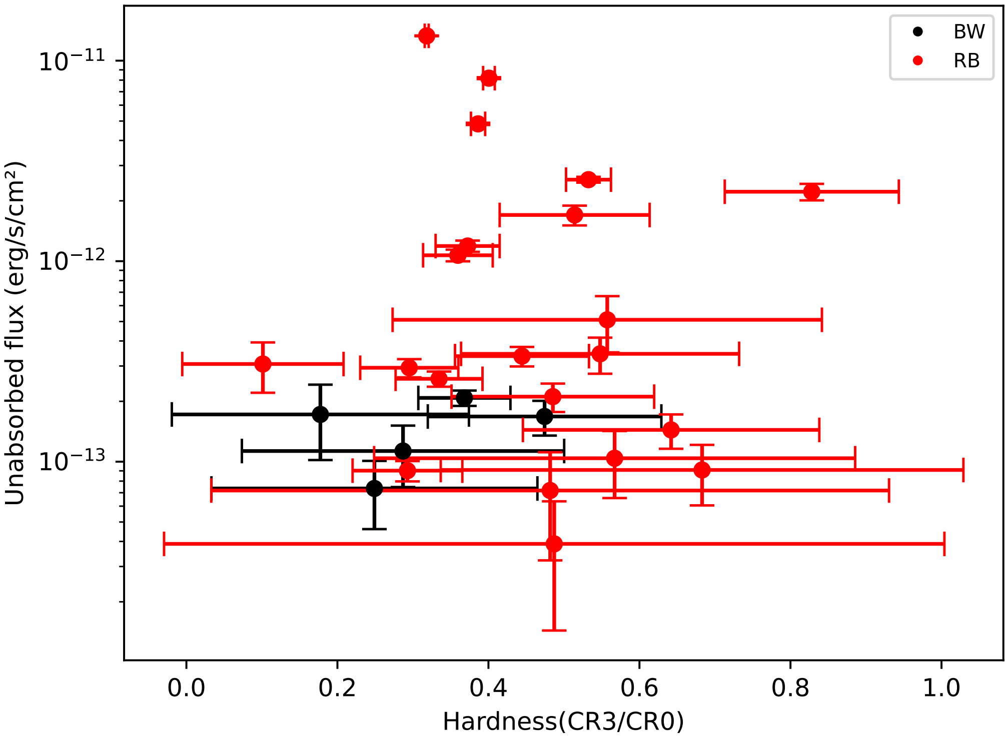

Figure 5.4: A Hardness flux diagram with errors from the result in the Swift results. CR3 is the count rate in the band 2-10 keV and CR0 is the total band from 0.3-10 keV. The fluxes from Swift are in the band total band 0.3-10 keV.

Name	d	CR0	err	CR3	err	F$_{U0}$/10^{-12}	10^{-12}err	UFL0/err
-	as	(c/s)	(c/s)	(c/s)	(c/s)	erg/s/cm^2	$erg/s/cm^2$	UFL0/err
J1124-3653	5.94	0.00221	0.000748	0.000634	0.00042	0.113	0.0383	3.0
J1301+0833	4.15	0.00151	0.000565	0.000376	0.000294	0.0735	0.02741	2.7
J1311-3430	1.85	0.00364	0.000321	0.00134	0.000188	0.208	0.01828	11.4
J1653-0159	0.55	0.00312	0.000616	0.00148	0.000384	0.168	0.03308	5.1
J2241-5236	3.19	0.00288	0.00118	0.000511	0.0005265	0.172	0.07014	2.5

Table 5.2: Swift results for black widows in table format.

Name	gmag	rmag	imag	zmag	ymag
B1957+20	20.9713	20.2651	19.8499	19.5979	19.6588
J0610-2100	-	-	21.5107	20.941	20.5393
J2051-0827	21.5732	20.4193	19.3906	18.8927	18.6408
J0636+5128	21.7412	21.7172	21.6289	20.8393	-
J0952-0607	22.1384	-	21.6377	-	-
J1221-0633	-	21.4909	20.1235	19.5292	19.1625
J1301+0833	-	-	21.5378	21.5348	-
J1317-0157	22.0652	21.8018	21.7883	-	-
J1555-2908	20.7155	20.4069	20.4143	18.5122	-
J1653-0159	20.8787	20.5009	20.0984	20.0302	19.7166
J1720-0534	-	21.5894	21.2807	20.8177	20.3719
J1731-1847	20.526	19.2972	18.6138	18.257	18.0398
J1805+0615	-	21.937	21.669	-	-
J1810+1744	20.101	20.2284	20.3329	20.4779	19.9431
J1928+1245	19.3589	18.319	17.8051	17.5087	17.2859
J2017-1614	-	22.0528	21.5359	-	-
J2047+1053	22.4241	22.0033	21.9032	-	-
J2052+1219	21.8554	22.3183	-	21.509	-
J2055+3829	-	21.1617	20.5616	20.102	19.6907
J2115+5448	-	-	21.8971	21.0558	-
J2214+3000	-	-	21.8726	-	20.1724
J2256-1024	21.8956	21.3172	20.9897	21.0346	-
J0336.0+7505	21.236	20.5934	20.6895	20.1496	-
J1406+1222	19.9162	19.951	19.3756	19.053	18.9262
J1408.6-2917	21.1343	21.1829	20.8663	20.263	-
J1838.2+3223	20.736	20.4663	20.4305	20.4655	-

Table 5.3: Pan-STARRS magnitudes for black widows in SpiderCat.

Name	gmag	rmag	imag	zmag	ymag
J0212+5320	14.7931	14.3882	14.1792	14.0563	14.1139
J0838-2827	20.6076	19.8339	19.2809	19.318	18.9204
J1023+0038	18.0534	16.6437	16.3047	17.0889	17.0898
J1048+2339	20.1084	19.2057	19.0691	18.8041	18.64
J1302-3258	-	-	20.8484	-	-
J1622-0315	19.6466	19.1631	18.9544	18.9544	18.876
J1628-3205	20.8019	-	-	-	-
J1723-2837	16.3427	15.5195	15.0823	14.8701	14.6654
J1816+4510	18.0731	18.3683	18.6033	18.8074	18.8736
J1908+2105	22.0652	20.931	20.2094	19.8519	19.6316
J1957+2516	18.9292	17.9174	17.3925	17.1181	16.8972
J2055+1545	21.0134	20.3931	20.2933	20.2725	19.9973
J2129-0429	17.4672	16.7174	16.4837	16.3609	16.239
J2215+5135	20.4088	19.6891	19.0514	18.8162	19.1906
J2339-0533	18.2508	19.5165	18.4974	17.8173	17.8751
J0523-2529	17.1861	16.5129	16.2069	16.0245	16.0222
J0935.3+0901	21.201	20.4939	20.4082	20.4113	20.0398
J1544-1128	19.2631	18.4562	18.2286	18.1941	18.0775
J2054.2+6904	20.8201	20.1174	19.7138	19.5555	19.3675
J0846.0+2820	16.2923	15.6699	15.3727	15.2393	15.0905

Table 5.4: Pan-STARRS magnitudes for redbacks in SpiderCat.

Chapter 6

Discussion

6.1 Overview Catalog

The SpiderCat catalog contains a total of 76 spider pulsars. Some of the systems in SpiderCat are not found in some of the databases that were queried. In Table 6.1, we see a summary of how many systems from SpiderCat appeared in each database.

The first note is that both SFD and HI4PI are full-sky surveys of the dust and gas in the Galaxy (see Chapter 3). As a consequence, all systems have a corresponding value as the entire sky has been mapped in these databases. For Bayestar, we see that some systems do not appear. This is because it is based on the Pan-STARRS survey which only covers north of DEC -30°. ATNF only contains spiders that have shown pulsations in the radio band, and this is not the case for the spider candidates. Therefore, none of the spider candidates are found in our ATNF search (Chapter 2). We can see a much higher number of exclusions for both Swift, Pan-STARRS and Gaia (Chapter 4 and 5 for details). These exclusions are due to a combination of magnitude or flux limits and sky coverage of each survey or catalog.

Database	black widows	redbacks	total
Basefile	40	36	76
ATNF	34	19	53
Gaia	12	31	43
Swift	5	21	26
Pan-STARRS	26	20	46
HI4PI	40	36	76
SFD	40	36	76
Bayestar19	35	18	53

Table 6.1: Summary of the number of spiders found in the different databases searched (as per 06.05.2024).

6.2 Highlights: the main results found in SpiderCat

As discussed in Section 2.4, from the timing properties collected in SpiderCat we have seen that spiders are among the fastest spinning NSs, with a P even shorter than that of other MSPs. This effect is highlighted in Figure 2.3, showing a histogram of the P for black widows, redbacks, and all MSPs. This is probably due to a longer or more efficient "spin-up" phase compared to other recycled MSPs. The "spin-up" phase in the life of a pulsar refers to a period during which the pulsar increases its rotational speed. In binary systems, a pulsar can accrete matter from its companion star. This happens when the companion star expands during its evolution and starts overflowing its Roche lobe. As material from the companion star accretes onto the pulsar, it brings angular momentum to the pulsar. This material generally forms an accretion disk as it spirals toward the

NS. The material in the accretion disk gradually spirals closer to the NS and eventually falls onto its surface. The angular momentum of the accreting material is transferred to the pulsar, causing it to spin faster.

As seen in Figure 3.2, we can clearly see a linear correlation between the reddening and the absorption along the different lines of sight for the spiders. This was a reaffirming discovery as both Foight et al. [32] and Predehl et al. [31] had made similar discoveries for the reddening and absorption, independent of the spiders that are in SpiderCat. The physical interpretation of this result is that the presence of larger dust particles and clouds also includes the presence of hydrogen gas clouds to a similar scale. This tells us that a particular concealer in the ISM does not exist alone. Another reason for this correlation is that the same assumptions were made for both properties. We used the total integrated density along the entire line of sight.

From Section 5.4, we showed two optical CMDs, and in both, we found a significant outlier in J1816, which showed a much bluer color than the other spiders. The bluer color comes from the companion temperature at 16000K [49]. This is a highly unusual companion for a redback, and the companion is suspected to be a proto-white dwarf. This elevation in the companion's temperature adequately explains the bluer color in the CMD, because most of the optical light emitted from a spider system is the blackbody radiation of the companion. And the blackbody radiation of higher temperature objects is shifted towards bluer wavelengths.

In Chapter 4 the main result was the proper motion discrepancy between the black widows and the redbacks. As both Figures 4.3 and 4.2 show, we can observe a higher total proper motion for the redbacks. For the redbacks, this does not seem to have a particular preference towards RA or DEC, which, of course, is reasonable as it is an Earthly coordinate system. The high proper motion for the redbacks could speak to a more violent supernova formation, leading to the redback systems having a higher tangential velocity through space as opposed to black widows.

The final highlight was from the X-ray counterparts identified by Swift. In Figure 5.4, we observe considerable uncertainties for all but three redbacks in both hardness and unabsorbed flux. It is also these three redbacks that we have identified as J1023+0038 [50, 51, 52, 53], J1227-4853 [53, 54] and J1544-1128 [55], in common for them all is that they are transitional MSPs. The redbacks have been observed in three different states. Given the high X-ray fluxes measured by Swift, we suspect that they occupied the more luminous disk state at the time.

6.3 Future work

Future updates for SpiderCat can be divided into two categories: maintenance and improvement.

From a maintenance perspective, the most important thing to do to improve the SpiderCat is to follow discoveries of spider systems. This also involves rerunning all scripts when a new system is discovered. If the system is not found in the different queries, the next step is to do an intensive literature search of the new system to see if other papers have made discoveries about it that are not yet included in the databases that the SpiderCat queries.

This thesis has focused primarily on data collection, verification and interpretation. The next natural step would be to present all these data to the community. For this, we have already begun developing a website that will interactively display the data I collected in SpiderCat (credit: Bogdan Voaidas).

There are also improvements to the data that could be collected. The first possible extension is the Shklovksii correction. This correction is due to the effect that proper motion has on the observed $\dot{P}$. The Shklovskii effect [56] can be described by,

$$\dot{P}_{obs} = \dot{P}_{intr} + \frac{P\mu^2 d}{c}. \tag{6.1}$$

With the Shklovskii correction, we could also include the intrinsic $\dot{E}$.

The second improvement that could be made are distance estimates. The distance estimates collected in SpiderCat are based on the YMW16 and NE2001 models. So, an improvement could be to make this estimation ourselves specifically for the spider population. In addition to the distance, one could then calculate the spider's luminosity. Collecting properties of the companion star could further improve the understanding of the interaction in the binary system. Data regarding the companion's base temperature, irradiated temperature and irradiating luminosity could give us a better understanding of the interaction in the binary system. In SpiderCat we have not quantified the time variability of fluxes in different bands. Introducing a time dependency to the fluxes or magnitudes would give a more complete view of spiders.

Finally, SpiderCat could be improved by querying several other sky maps or catalogs in several bands. Firstly, this would be the γ-band, as this is not included in the current version of SpiderCat. Databases that could also be queried are eROSITA in X-rays [57], 4FGL [58], 3PC [59] in gamma-rays, SDSS in optical [60] and WISE in the infrared [61].

References

[1] Hewish, A. and Bell, S. J. and Pilkington, J. D. H. and Scott, P. F. and Collins, R. A.. 'Observation of a Rapidly Pulsating Radio Source'. In: *Nature* 217 (1968), pp. 615–618.

[2] Joonas Nättilä and Jari J. E. Kajava. 'Fundamental Physics with Neutron Stars'. In: *Handbook of X-ray and Gamma-ray Astrophysics*. Springer Nature Singapore, Nov. 2022, pp. 1–53. ISBN: 9789811645440. DOI: 10.1007/978-981-16-4544-0_105-1. URL: http://dx.doi.org/10.1007/978-981-16-4544-0_105-1.

[3] A. Heger. 'How Massive Single Stars End Their Lifes'. In: *The Astrophysical Journal* 591 (2022), p. 288.

[4] A.Y. Potekhin P. Haensel and D.G. Yakovlev. *Neutron Stars 1: Equation of State and Structure*. Springer Science+Business Media, 2007.

[5] J. M. Lattimer and M. Prakash. 'Neutron star structure and the equation of state'. In: *The Astrophysical Journal* 550 (2001), pp. 426–442.

[6] D. C.. Backer. 'A millisecond pulsar'. In: *Nature* 300 (1982), pp. 615–618.

[7] NASA. *Large Area Telescope*. https://fermi.gsfc.nasa.gov/science/instruments/lat.html. Accessed: 2023-04-17. 2023.

[8] Duncan Lorimer. *Galactic Millisecond Pulsars*. URL: http://astro.phys.wvu.edu/GalacticMSPs/ (visited on 27th Feb. 2024).

[9] Benvenuto, O. G., De Vito, M. A. and Horvath, J. E. 'Evolution of redback radio pulsars in globular clusters'. In: *Astronomy and Astrophysics* 598 (2017), A35. DOI: 10.1051/0004-6361/201628692. URL: https://doi.org/10.1051/0004-6361/201628692.

[10] Phys.org. *Exploring the origin of 'black widow' pulsars*. https://phys.org/news/2022-07-exploring-black-widow-pulsars.html. Accessed: 2024-04-23. July 2022.

[11] R. N. Manchester et al. 'The Australia Telescope National Facility Pulsar Catalogue'. In: *Astrophysical Jornal* 129.4 (Apr. 2005), pp. 1993–2006. DOI: 10.1086/428488. arXiv: astro-ph/0412641 `[astro-ph]`.

[12] Karen I. Perez et al. 'Green Bank Telescope Discovery of the Redback Binary Millisecond Pulsar PSR J0212+5321'. In: *The Astrophysical Journal* 952.2 (July 2023), p. 150. ISSN: 1538-4357. DOI: 10.3847/1538-4357/acdc23. URL: http://dx.doi.org/10.3847/1538-4357/acdc23.

[13] Paulo Freire. *Pulsars in Globular Clusters*. URL: https://www3.mpifr-bonn.mpg.de/staff/pfreire/GCpsr.html (visited on 27th Feb. 2024).

[14] Swinburne University of Technology. *Pulsar dispersion measure*. URL: https://astronomy.swin.edu.au/cosmos/p/pulsar+dispersion+measure (visited on 7th Mar. 2024).

[15] Swinburne University of Technology. *Ascending Node*. https://astronomy.swin.edu.au/cosmos/a/ascending+node. Accessed: 2023-04-17. 2023.

[16] F. Özel and P. Freire. 'Masses, Radii, and the Equation of State of Neutron Stars'. In: *Annual Review of Astronomy and Astrophysics* 54 (Sept. 2016), pp. 401–440. DOI: 10.1146/annurev-astro-081915-023322. arXiv: 1603.02698 `[astro-ph.HE]`.

[17] D. R. Lorimer and M. Kramer. *Handbook of Pulsar Astronomy*. Vol. 4. 2004.

[18] psrqpy Development Team. *psrqpy: A Python Package for Querying the ATNF Pulsar Catalogue*. https://psrqpy.readthedocs.io/en/latest/. Accessed: 2023-04-17. 2023.

[19] A. M. Archibald et al. 'A Radio Pulsar/X-ray Binary Link'. In: *The Astrophysical Journal Letters* 786.1 (2014), p. L7. DOI: 10.1088/2041-8205/786/1/L7. URL: https://iopscience.iop.org/article/10.1088/2041-8205/786/1/L7/meta.

[20] J. W. T. Hessels et al. 'A Radio Pulsar/X-ray Binary Link'. In: *The Astrophysical Journal* 775.1 (2013), p. 27. DOI: 10.1088/0004-637X/775/1/27. URL: https://iopscience.iop.org/article/10.1088/0004-637X/775/1/27/meta.

[21] CSIRO. *ATNF Pulsar Catalogue*. URL: https://www.atnf.csiro.au/research/pulsar/psrcat/ (visited on 27th Feb. 2024).

[22] N. Ben Bekhti et al. 'HI4PI: a full-sky Hi survey based on EBHIS and GASS'. In: *Astronomy amp; Astrophysics* 594 (Oct. 2016), A116. ISSN: 1432-0746. DOI: 10.1051/0004-6361/201629178. URL: http://dx.doi.org/10.1051/0004-6361/201629178.

[23] David J. Schlegel, Douglas P. Finkbeiner and Marc Davis. 'Maps of Dust Infrared Emission for Use in Estimation of Reddening and Cosmic Microwave Background Radiation Foregrounds'. In: *The Astrophysical Journal* 500.2 (June 1998), pp. 525–553. ISSN: 1538-4357. DOI: 10.1086/305772. URL: http://dx.doi.org/10.1086/305772.

[24] Gregory M. Green et al. 'A THREE-DIMENSIONAL MAP OF MILKY WAY DUST'. In: *The Astrophysical Journal* 810.1 (Aug. 2015), p. 25. ISSN: 1538-4357. DOI: 10.1088/0004-637x/810/1/25. URL: http://dx.doi.org/10.1088/0004-637X/810/1/25.

[25] C. Clayton Geoffery, A. Cardelli Jason and S. Mathis John. 'Relationship between Infrared, Optical, and Ultraviolet Extinction'. In: *Astrophysical Journal* 345 (1988), p. 245.

[26] Institute for Astronomy, University of Hawaii. *Pan-STARRS (Panoramic Survey Telescope and Rapid Response System)*. http://www2.ifa.hawaii.edu/research/Pan-STARRS.shtml. Accessed: 2024-04-23. 2024.

[27] Hale Bradt. *Astronomy Methods: A Physical Approach to Astronomical Observations*. Cambridge: Cambridge University Press, 2004.

[28] High Energy Astrophysics Science Archive Research Center (HEASARC). *HEASoft: Unified Release of FTOOLS and XANADU*. https://heasarc.gsfc.nasa.gov/lheasoft/download.html. Accessed: 2024-04-23. 2024.

[29] J. M. Yao, R. N. Manchester and N. Wang. 'A New Electron-density Model for Estimation of Pulsar and FRB Distances'. In: *Astrophysical journal* 835.1, 29 (Jan. 2017), p. 29. DOI: 10.3847/1538-4357/835/1/29. arXiv: 1610.09448 [astro-ph.GA].

[30] J. M. Cordes and T. J. W. Lazio. *NE2001.I. A New Model for the Galactic Distribution of Free Electrons and its Fluctuations*. 2003. arXiv: astro-ph/0207156 [astro-ph].

[31] P. Predehl and J. H. M. M. Schmitt. 'X-raying the interstellar medium: ROSAT observations of dust scattering halos.' In: *Astronomy and Astrophysics* 293 (Jan. 1995).

[32] D. R. Foight et al. 'Probing X-RAY absorption and optical extinction in the interstellar medium using Chandra observations of supernova remnants'. In: *The Astrophysical Journal* 826.1 (2016), p. 66. DOI: 10.3847/0004-637X/826/1/66. URL: https://iopscience.iop.org/article/10.3847/0004-637X/826/1/66.

[33] Orellana, G. et al. 'Molecular gas, dust, and star formation in galaxies - I. Dust properties and scalings in 1600 nearby galaxies'. In: *Astronomy and Astrrophysics* 602 (2017), A68. DOI: 10.1051/0004-6361/201629009. URL: https://doi.org/10.1051/0004-6361/201629009.

[34] European Space Agency. *Proper motion – Gaia*. Accessed: 2023-04-17. 2023.

[35] European Space Agency. *Gaia – Mapping the stars of the Milky Way*. https://www.esa.int/Science_Exploration/Space_Science/Gaia. Accessed: 2023-04-17. 2023.

[36] T. Prusti et al. 'TheGaiamission'. In: *Astronomy and Astrophysics* 595 (Nov. 2016), A1. ISSN: 1432-0746. DOI: 10.1051/0004-6361/201629272. URL: http://dx.doi.org/10.1051/0004-6361/201629272.

[37] Gaia Collaboration et al. 'Gaia Data Release 3. Summary of the content and survey properties'. In: 674, A1 (June 2023), A1. DOI: 10.1051/0004-6361/202243940. arXiv: 2208.00211 [astro-ph.GA].

[38] C. A. L. Bailer-Jones et al. ‘Estimating Distances from Parallaxes. V. Geometric and Photogeometric Distances to 1.47 Billion Stars in Gaia Early Data Release 3’. In: *The Astronomical Journal* 161.3 (Feb. 2021), p. 147. ISSN: 1538-3881. DOI: 10.3847/1538-3881/abd806. URL: http://dx.doi.org/10.3847/1538-3881/abd806.

[39] D. C. Price, C. Flynn and A. Deller. ‘A comparison of Galactic electron density models using PyGEDM’. In: *Publications of the Astronomical Society of Australia* 38 (2021). ISSN: 1448-6083. DOI: 10.1017/pasa.2021.33. URL: http://dx.doi.org/10.1017/pasa.2021.33.

[40] W. J. Cocke, M. J. Disney and D. J. Taylor. ‘Discovery of Optical Signals from Pulsar NP 0532’. In: *Nature* 221.5180 (1969), pp. 525–527. ISSN: 1476-4687. DOI: 10.1038/221525a0. URL: https://doi.org/10.1038/221525a0.

[41] P. T. Wallace et al. ‘Detection of optical pulses from the Vela pulsar’. In: *Nature* 266.5604 (1977), pp. 692–694. ISSN: 1476-4687. DOI: 10.1038/266692a0. URL: https://doi.org/10.1038/266692a0.

[42] Nicholas Kaiser. ‘Pan-STARRS: a wide-field optical survey telescope array’. In: *Ground-based Telescopes*. Ed. by Jacobus M. Oschmann Jr. Vol. 5489. International Society for Optics and Photonics. SPIE, 2004, pp. 11–22. DOI: 10.1117/12.552472. URL: https://doi.org/10.1117/12.552472.

[43] Space Telescope Science Institute. *PS1 Filter Properties*. https://outerspace.stsci.edu/display/PANSTARRS/PS1+Filter+properties. Accessed: 2024-04-23. 2024.

[44] H. A. Flewelling et al. ‘The Pan-STARRS1 Database and Data Products’. In: *The Astrophysical Journal Supplement Series* 251.1 (Oct. 2020), p. 7. ISSN: 1538-4365. DOI: 10.3847/1538-4365/abb82d. URL: http://dx.doi.org/10.3847/1538-4365/abb82d.

[45] J. L. Tonry et al. ‘The Pan-STARRS1 Photometric System’. In: *The Astrophysical Journal* 750.2, 99 (May 2012), p. 99. DOI: 10.1088/0004-637X/750/2/99. arXiv: 1203.0297 [astro-ph.IM].

[46] Karri I. I. Koljonen and Manuel Linares. ‘A Gaia view of the optical and X-ray luminosities of compact binary millisecond pulsars’. In: *Astrophysics* (2023). arXiv: 2308.07377 [astro-ph.HE].

[47] NASA Goddard Space Flight Center. *The Neil Gehrels Swift Observatory*. https://swift.gsfc.nasa.gov/. Accessed: 2024-04-23. 2024.

[48] P. A. Evans et al. ‘2SXPS: An Improved and Expanded Swift X-Ray Telescope Point-source Catalog’. In: *The Astrophysical Journal Supplement Series* 247.2 (Apr. 2020), p. 54. ISSN: 1538-4365. DOI: 10.3847/1538-4365/ab7db9. URL: http://dx.doi.org/10.3847/1538-4365/ab7db9.

[49] D. L. Kaplan et al. ‘Discovery of the Optical/Ultraviolet/Gamma-Ray Counterpart to the Eclipsing Millisecond Pulsar J1816+4510’. In: *The Astrophysical Journal* 753, 174 (2012), p. 174. DOI: 10.1088/0004-637X/753/2/174. arXiv: 1205.3699 [astro-ph.HE].

[50] P. H. T. Tam et al. ‘Evidence for Gamma-ray Emission from the Low-mass X-ray Binary System First J102347.6+003841’. In: *Astrophysical Journal* 724 (2010), pp. L207–L211. DOI: 10.1088/2041-8205/724/2/L207. arXiv: 1010.4311 [astro-ph.HE].

[51] B. W. Stappers et al. ‘A State Change in the Missing Link Binary Pulsar System PSR J1023+0038’. In: *Astrophysical Journal* 790, 39 (2014), p. 39. DOI: 10.1088/0004-637X/790/1/39. arXiv: 1311.7506 [astro-ph.HE].

[52] A. Patruno et al. ‘A New Accretion Disk around the Missing Link Binary System PSR J1023+0038’. In: *Astrophysical journal* 781, L3 (2014), p. L3. DOI: 10.1088/2041-8205/781/1/L3. arXiv: 1310.7549 [astro-ph.HE].

[53] M. Linares. ‘X-ray states of redback millisecond pulsars’. In: *Astrophysical Journal* 795, 72 (2014), p. 72. DOI: 10.1088/0004-637X/795/1/72. arXiv: 1406.2384 [astro-ph.HE].

[54] J. Roy et al. ‘Discovery of Psr J1227-4853: A Transition from a Low-mass X-Ray Binary to a Redback Millisecond Pulsar’. In: *Astrophysical Journal* 800, L12 (Feb. 2015), p. L12. DOI: 10.1088/2041-8205/800/1/L12. arXiv: 1412.4735 [astro-ph.HE].

[55] S. Bogdanov and J. P. Halpern. ‘Identification of the High-energy Gamma-Ray Source 3FGL J1544.6-1125 as a Transitional Millisecond Pulsar Binary in an Accreting State’. In: *Astrophysical Journal* 803, L27 (Apr. 2015), p. L27. DOI: 10.1088/2041-8205/803/2/L27. arXiv: `1503.01698 [astro-ph.HE]`.

[56] I. S. Shklovskii. ‘Possible Causes of the Secular Increase in Pulsar Periods.’ In: *Soviet Astronomy* 13 (Feb. 1970), p. 562.

[57] Max-Planck Institute for Extraterrestrial Physics. *eROSITA-DE: Main Website*. https://erosita.mpe.mpg.de/. Accessed: 2024-04-23. 2024.

[58] Fermi Gamma-ray Space Telescope. *LAT 12-year Source Catalog (4FGL-DR3)*. https://fermi.gsfc.nasa.gov/ssc/data/access/lat/12yr_catalog/. Accessed: 2024-04-23. 2024.

[59] Fermi Gamma-ray Space Telescope. *LAT Third Catalog of Gamma-ray Pulsars*. https://fermi.gsfc.nasa.gov/ssc/data/access/lat/3rd_PSR_catalog/. Accessed: 2024-04-23. 2024.

[60] SDSS-III Collaboration. *SDSS DR8 Spectroscopic Catalogs*. https://www.sdss3.org/dr8/spectro/catalogs.php. Accessed: 2024-04-23. 2024.

[61] Edward L. Wright et al. ‘The Wide-field Infrared Survey Explorer (WISE): Mission Description and Initial On-orbit Performance’. In: *Astrophysical Journal* 140.6 (Dec. 2010), pp. 1868–1881. DOI: 10.1088/0004-6256/140/6/1868. arXiv: `1008.0031 [astro-ph.IM]`.

NTNU

Norwegian University of
Science and Technology